Multiple Hydrometeors All-Sky Microwave Radiance Assimilation in FV3GFS

Mingjing Tong,[a,b] Yanqiu Zhu,[c] Linjiong Zhou,[b,d] Emily Liu,[e] Ming Chen,[f]
Quanhua Liu,[g] and Shian-Jiann Lin[b]

[a] *SAIC, Princeton, New Jersey*
[b] *NOAA/GFDL, Princeton, New Jersey*
[c] *I.M. Systems Group, NCEP Environmental Modeling Center, College Park, Maryland*
[d] *Program in Atmospheric and Oceanic Sciences, Princeton University, Princeton, New Jersey*
[e] *SRG, NCEP Environmental Modeling Center, College Park, Maryland*
[f] *NESDIS, and University of Maryland, College Park, College Park, Maryland*
[g] *NESDIS/STAR, College Park, Maryland*

ABSTRACT

Motivated by the use of the GFDL microphysics scheme in the Finite-Volume Cubed-Sphere Dynamical Core Global Forecast System (FV3GFS), the all-sky radiance assimilation framework has been expanded to include precipitating hydrometeors. Adding precipitating hydrometeors allows the assimilation of precipitation-affected radiance in addition to cloudy radiance. In this upgraded all-sky framework, the five hydrometeors, including cloud liquid water, cloud ice, rain, snow, and graupel, are the new control variables, replacing the original cloud water control variable. The Community Radiative Transfer Model (CRTM) was interfaced with the newly added precipitating hydrometeors. Subgrid cloud variability was considered by using the average cloud overlap scheme. Multiple scattering radiative transfer was activated in the upgraded framework. Radiance observations from the Advanced Microwave Sounding Unit-A (AMSU-A) and the Advanced Technology Microwave Sounder (ATMS) over ocean were assimilated in all-sky approach. This new constructed all-sky framework shows neutral to positive impact on overall forecast skill. Improvement was found in 500-hPa geopotential height forecast in both Northern and Southern Hemispheres. Temperature forecast was also improved at 850 hPa in the Southern Hemisphere and the tropics.

1. Introduction

In recent years, the main trend of making use of satellite data in numerical weather prediction (NWP) is the assimilation of cloud- and precipitation-affected radiances. Research efforts have been devoted to improving observation error modeling (Geer and Bauer 2011; Okamoto et al. 2014; Minamide and Zhang 2017), radiative transfer models (e.g., Geer et al. 2009; Geer and Baordo 2014; Sieron et al. 2017; Stegmann et al. 2018; Sieron et al. 2018), and parameterizations of cloud and precipitation in forecast model (e.g., Forbes et al. 2016). The first operational implementation of all-sky microwave radiance assimilation was achieved at the European Centre

for Medium-Range Weather Forecasts (ECMWF) in 2009, with observations from the Special Sensor Microwave Imager (SSM/I) and Advanced Microwave Scanning Radiometer for the Earth Observing System (AMSR-E) assimilated in all-sky approach (Bauer et al. 2010). Since then, radiances from more microwave imagers and sounders have been assimilated in all-sky conditions in their 4D-Var system (Geer et al. 2018). Geer et al. (2017) shows that assimilation of microwave radiances sensitive to cloud and precipitation has contributed to the ECMWF's forecast skill improvement. The Japan Meteorological Agency (JMA) has been developing the assimilation all-sky microwave and infrared radiances in their global data assimilation system (Kazumori and Kadowaki 2017; Okamoto 2013). In their recent study, the assimilation of all-sky microwave radiances improved analysis and first guess fields. Positive impact was also observed in tropical cyclone (TC) intensity analysis and prediction (Kazumori and Kadowaki 2017). Hydrometeors are not control variables in the 4D-Var

---

Corresponding author: Dr. Mingjing Tong, mingjing.tong@noaa.gov

systems of ECMWF and JMA (Geer et al. 2018). The tangent linear of the forecast model in 4D-Var system provide the link between the change in hydrometeors and the change in control variables at observation time (Geer et al. 2018). A single moist control variable, which covers water vapor, liquid, and frozen cloud water, is used in the Met Office operational system for the assimilation of humidity- and cloud-sensitive observations (Ingleby et al. 2013; Migliorini et al. 2017). A moisture-incrementing operator has been developed and improved to partition the total water increments into its three phases (Migliorini et al. 2017).

Nonprecipitating cloudy radiances from the Advanced Microwave Sounding Unit-A (AMSU-A) microwave radiometer have been assimilated into NCEP's Global Forecast System (GFS) since 2016 (Zhu et al. 2016). More recently, the all-sky approach has been expanded to the assimilation of the nonprecipitating cloudy radiances from the Advanced Technology Microwave Sounder (ATMS) (Zhu et al. 2019). Precipitation-affected radiances have not been assimilated in the operational GFS Global Data Assimilation System (GDAS), mainly because the cloud microphysics parameterization scheme (Zhao and Carr 1997; Moorthi et al. 2001) used in the original Global Spectral Model (GSM)-based GFS does not provide precipitation information in the model output. Cloud water, which covers cloud liquid water and cloud ice, is the only cloud-related prognostic variable in the GSM-based GFS. Cloud water is a control variable in the all-sky radiance assimilation framework of GFS (Zhu et al. 2016).

The Finite-Volume Cubed-Sphere Dynamical Core (FV3) (Lin 1997, 2004; Putman and Lin 2007) developed at the National Oceanic and Atmospheric Administration (NOAA) Geophysical Fluid Dynamics Laboratory (GFDL) was selected to be the dynamical core of the next-generation global and regional forecast systems at NCEP. The FV3 dynamical core coupled to the operational GFS physics package was built at GFDL. This new global model was embedded into the NOAA Environment Modeling System (NEMS) and coupled to the data assimilation system at the NCEP Environmental Modeling Center (EMC). This next-generation global forecast system called FV3GFS became operational in June 2019.

One of the major model upgrades for this 2019 version (FY19) of FV3GFS is the replacing of the Zhao–Carr cloud microphysics scheme (Zhao and Carr 1997; Moorthi et al. 2001) in the GFS physics package with the GFDL cloud microphysics scheme (Zhou et al. 2019). This model physics upgrade improves the global anomaly correlation coefficients (ACC) of geopotential height at 500 hPa as well as tropical cyclone track and intensity forecast (Chen et al. 2019a,b). Another potential benefit of this microphysics upgrade is that it provides not only cloud but also precipitation related prognostic variables. This opens the door for the assimilation of precipitation-affected radiance.

In this study, we expanded the all-sky radiance assimilation framework for the FV3GFS to include all hydrometeors associated with the upgraded microphysics scheme, particularly the precipitating hydrometeors. The individual hydrometeors were chosen to be the new control variables. Both static background error variance and ensemble perturbations were augmented for the new control variables. The radiative transfer model was interfaced with the newly added precipitating hydrometeors. A few experiments were conducted to evaluate the performance of the upgraded all-sky radiance assimilation framework and the impact of assimilating precipitation-affected radiances.

The paper is organized as follows: The FV3GFS data assimilation system and the original all-sky radiance assimilation framework are briefly described in section 2. The expansion of the all-sky radiance assimilation framework with precipitating hydrometeors included is described in section 3. The design of the experiments and the impacts on analysis and forecast are presented in section 4. Conclusions and future work are summarized in section 5.

2. The original all-sky radiance assimilation framework in FV3GFS

a. The FV3GFS data assimilation system

The data assimilation system for the FV3GFS is largely inherited from the GSM-based GFS with some enhancement added. Observations in the 6-h window centered at synoptic time are assimilated with a hybrid 4D ensemble–variational data assimilation method (4DEnVar; Wang and Lei 2014; Kleist and Ide 2015). The description of the hybrid 4DEnVar system here mainly follows Kleist and Ide (2015). The system utilizes a dual-resolution configuration. The high-resolution deterministic forecast is updated by the Gridpoint Statistical Interpolation (GSI; Kleist et al. 2009a) variational analysis through a linear combination of the increment derived from a static background error covariance and the increment derived from the ensemble perturbations. The weight given to the static and the ensemble contributions to the increment are 12.5% and 87.5%, respectively. The ensemble is updated using an ensemble square root filter (EnSRF; Whitaker and Hamill 2002;

Whitaker et al. 2008). The horizontal resolution[1] of the FY19 FV3GFS is C768 (~13 km) for the deterministic forecast and C384 (~25 km) for the ensemble forecast. The model has 64 vertical levels with the model top at 0.2 hPa. Both GSI and EnSRF analyses are performed on Gaussian grid at half of the resolution of the deterministic forecast, which corresponds to C384 with 1536 × 768 grid points. The analysis increments on the Gaussian grid are remapped to the cubed-sphere grid inside the model to initialize the forecast. The tangent-linear normal mode constraint (Kleist et al. 2009b) is utilized to improve the balance of the GSI analysis. The multiplicative inflation by relaxation to the prior spread (Whitaker and Hamill 2012) is used to account for underrepresented sources of background error in the EnSRF. In addition to multiplicative inflation, the stochastically perturbed parameterization tendency scheme (SPPT; Buizza et al. 1999) and the stochastically perturbed boundary layer humidity scheme (SHUM; Tompkins and Berner 2008) are employed to address sampling error due to model uncertainties.

b. The original all-sky radiance assimilation framework

The all-sky radiance assimilation framework developed for the GSM GFS is adopted for the first implementation of FV3GFS. The technique details of the all-sky approach are documented in Zhu et al. (2016, 2019). Here we provide a few key aspects of the original all-sky framework with the descriptions derived from Zhu et al. (2016, 2019), in order to facilitate the introduction of the expanded all-sky framework later. Although the FV3GFS with the GFDL microphysics has prognostic variables for cloud liquid water, cloud ice, rain, snow, and graupel, the normalized cloud water mixing ratio (CW) is still used as the control variable. The normalized CW is defended as the sum of the cloud liquid water mixing ratio (Ql) and cloud ice mixing ratio (Qi) normalized by its background error standard deviation. The Community Radiative Transfer Model (CRTM) requires profiles of individual hydrometeors as input. The first guess of CW is partitioned into Ql and Qi based on temperature [Eq. (1) in Zhu et al. 2019]. Incremental conversion between cloud control variable (CW) and cloud state variables (Ql and Qi) through the tangent linear and adjoint of the decomposition operator is required at each inner loop iteration (Zhu et al. 2019).

The static background error standard deviation of CW is set to be 5% of its first guess (Zhu et al. 2016). The static error covariance does not provide the cross-covariances between CW and other control variables. Flow-dependent error covariances including cross-covariances are provided by the ensemble, which plays more important role in the analysis.

Due to the choice of the cloud control variable in current all-sky assimilation framework of FV3GFS, the analysis increments of precipitating hydrometeors are not available. It may not be ideal to partially update cloud state variables. Therefore, the analysis increments of Ql and Qi decomposed from the increment of CW are not used to update the model initial condition. Even without updating cloud variables, radiances affected by cloud can still have explicit impact on temperature and moisture, and indirect impact on wind through the correlation derived from the ensemble.

Ocean field-of-view (FOV) radiances from all AMSU-A and ATMS channels, except AMSU-A channel 14 and ATMS channel 15, are assimilated in all-sky conditions in the FY19 FV3GFS. AMSU-A channel 14 and ATMS channel 15 are high peaking channels. The model top and vertical levels cannot provide adequate atmospheric state profiles at high altitudes for these two channels; therefore, they are not assimilated in the FY19 FV3GFS. More channel information of AMSU-A and ATMS can be found in Table 2 of Zhu et al. (2019). Since precipitating hydrometeors are not included in the original all-sky framework, precipitation-affected radiances are screened out in data thinning and quality control procedures. More details about precipitation screening can be found in Zhu et al. (2016).

The CRTM (Han et al. 2006; Liu and Boukabara 2014) developed at the Joint Center for Satellite Data Assimilation (JCSDA) is used as the observation operator for radiance data in NCEP's data assimilation system. The CRTM, version 2.2.3, is used in the original all-sky framework of the FY19 FV3GFS. Without passing precipitating profiles into the CRTM, multiple scattering is not activated, and radiative transfer is solved in emission mode.

3. Expansion of the all-sky framework to the assimilation of precipitation-affected radiance

In the new all-sky radiance assimilation framework, the model state variables and the control variables were augmented to include rain, snow, and graupel in addition to cloud liquid water and cloud ice in both GSI and EnSRF analysis systems. We decided to use the five individual hydrometeors as the new control variables because it is more straightforward to implement and does

---

[1] The resolution of the cubed-sphere grid is defined as the number of finite-volume cells on each tile of the cubed sphere. For example, C384 means 384 × 384 finite-volume cells on each tile of the cubed sphere.

not require cloud decomposition and associated tangent linear and adjoin operators. Similar to the original all-sky framework, the mixing ratios of each individual hydrometeors normalized by their background error standard deviations were treated as control variables. The static background error variances for the individual hydrometeors were constructed the same way as the CW background error variance. Namely, the background error standard deviation was specified to be 5% of the first guess of the hydrometeor mixing ratios. The cross-covariances came from the ensemble, which was also expanded to include perturbations from precipitating hydrometeors. The analysis increments of the hydrometeors can now be used to update the model state to initialize the forecast.

To assimilate precipitation-affected radiances in this new framework, precipitation screening was removed in both data thinning and quality control procedures. The original bias correction scheme documented in Zhu et al. (2014a,b) was adopted. The bias correction coefficients need to be spun up by the new system itself. We monitored the simulated brightness temperature before and after bias correction to ensure that the bias correction scheme worked effectively. More details about interfacing the radiative transfer model, estimating observation errors, and changes made in quality control will be described in the following sections.

a. Radiative transfer model

In the presence of precipitation, multiple scattering is activated in radiative transfer because of significant scattering effects from snow and graupel. In this study, the advanced doubling-adding (ADA) method (Liu and Weng 2006) was chosen to solve the radiative transfer equation under scattering condition. The number of streams required to perform radiative transfer in multiple-scattering atmosphere is determined inside CRTM based on the Mie size parameter $2\pi r/\lambda$, where r is the largest effective radius of the scattering hydrometers and λ is the wavelength of the incident electromagnetic radiation. The hydrometeor optical properties including mass extinction coefficient ($m^2\,kg^{-1}$), single-scattering albedo and phase function coefficients, which are required by the ADA solver, are read from lookup tables (LUTs). During radiative transfer calculation, the optical properties are interpolated from the LUTs based on input frequency and hydrometeor effective radius. Only liquid species are temperature dependent. The type of solid species is determined from the input bulk density. In the officially released CRTM LUTs for cloud liquid water, cloud ice, rain, snow, and graupel, the optical properties were obtained by representing the species as spherical particles (Liu and Weng 2006). The Fast Microwave
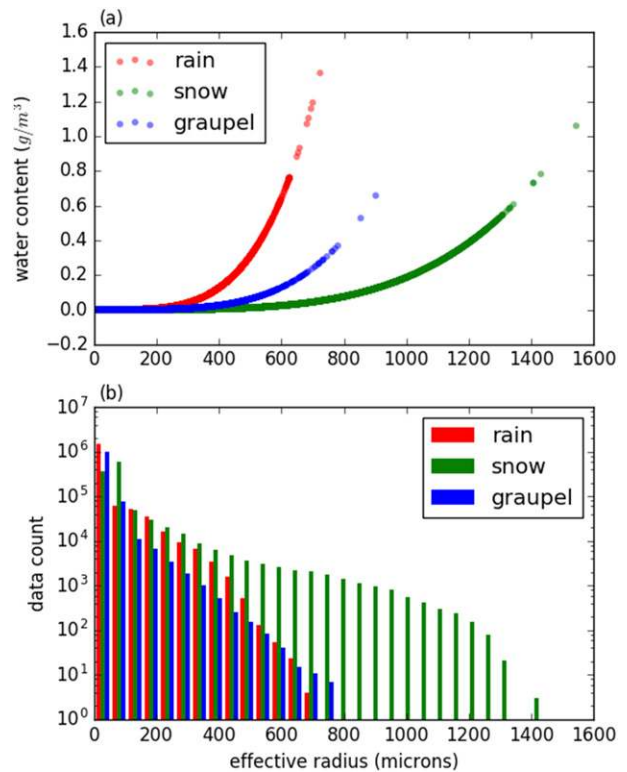

FIG. 1. (a) Scatterplot of effective radius (μm) as a function of water content (g m^{-3}), and (b) number of observations in log scale classified into 50-μm effective radius bins from a single analysis on 0000 UTC 15 Jul 2017.

Emissivity Model, version 6 (FASTEM-6) (English and Hewison 1998; Liu et al. 2011; Bormann et al. 2012; Kazumori and English 2015), is employed to compute microwave ocean surface emissivity.

When using CRTM in data assimilation, the K-matrix functions are used to compute the model brightness temperature and its Jacobians (sensitivities of brightness temperature to atmospheric and surface parameters) by taking inputs of atmospheric profiles and surface properties. The hydrometeor water path of each layer ($kg\,m^{-2}$) and effective radius, which are used to determine cloud and precipitation radiative properties, need to be passed into the CRTM. The effective radii of cloud liquid water and cloud ice are hard coded to be 5 μm in the CRTM. Based on some observational studies (e.g., Martin et al. 1994; Heymsfield and McFarquhar 1996; Donovan 2003) and comparing to the values used in different forecast models (Martin et al. 1994), 5 μm may be too small, especially for cloud ice. We modified the CRTM code to allow the effective radii of cloud liquid water and cloud ice to vary, and computed the effective radii of the two species based on formulas in a few parameterization studies, including Martin et al. (1994) for
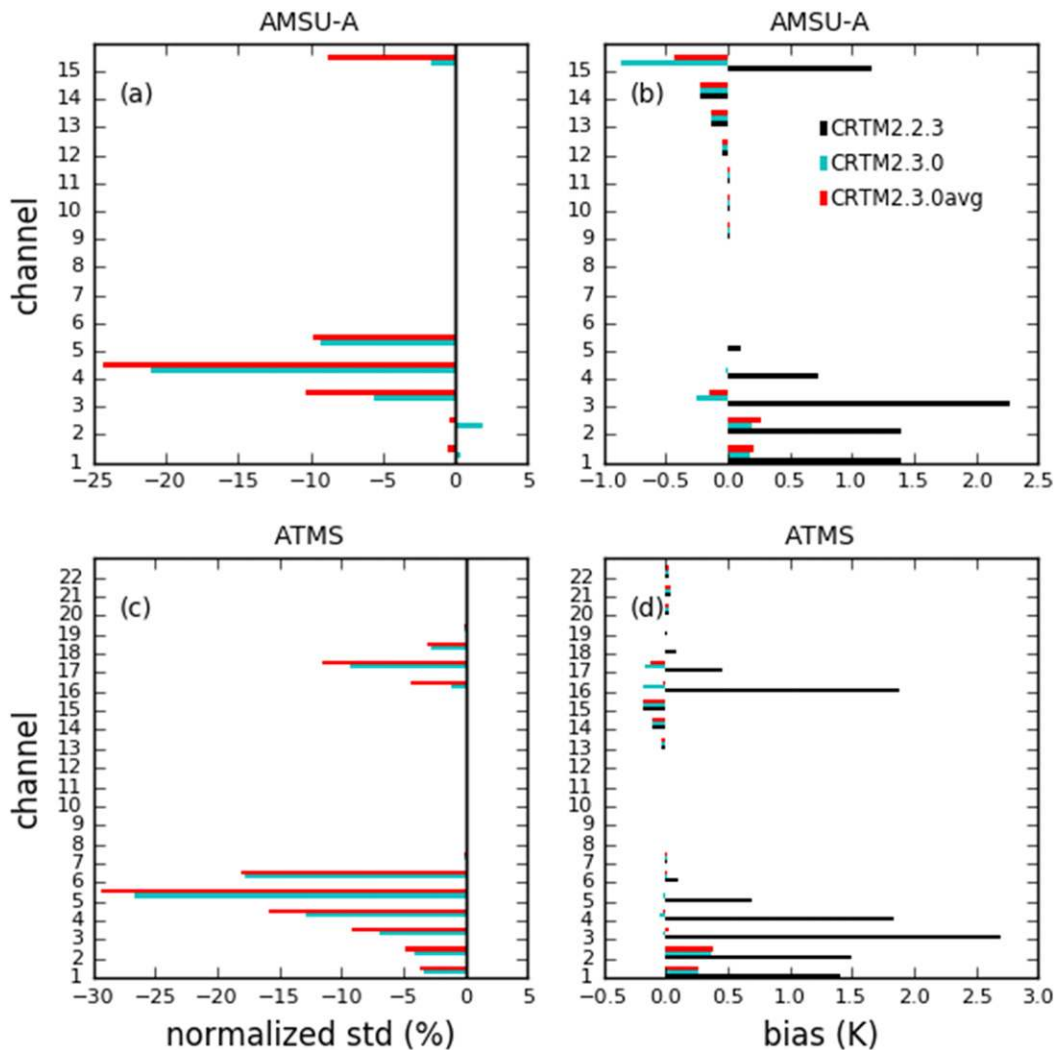
FIG. 2. Comparing OmF of simulations using different CRTM configurations. CRTM2.2.3: using CRTM 2.2.3 assuming overcast; CRTM2.3.0: using CRTM 2.3.0 assuming overcast; CRTM2.3.0avg: using CRTM 2.3.0 with averaged cloud overlap scheme. (left) OmF standard deviations of CRTM2.3.0 and CRTM2.3.0avg normalized by the OmF standard deviation of CRTM2.2.3. (right) OmF bias. (a),(b) OmF statistics of AMSU-A (including *NOAA-15*, *NOAA-18*, *NOAA-19*, and *MetOp-A*) channels; (c),(d) OmF statistics of ATMS (*SNPP*) channels. Statistics were computed from the same observations passed quality control in all of the three simulations over ocean using the same first guess forecasts for the period from 0000 UTC 10 Jul to 1800 UTC 20 Jul 2017.

liquid water and Heymsfield and McFarquhar (1996) for cloud ice. However, the changes led to worse first guess (FG) fit to observations. Therefore, we decided to keep using the default 5 μm for cloud liquid water and cloud ice in this study, and will investigate more on this, when we explore better optical properties for different species in the future. For the other three precipitating hydrometeors, the effective radii were calculated based on the ratio of the third and second moments of the particle size distribution following Hansen and Travis (1974):

$$r_{\text{eff}} = \frac{\int r^3 N(r)\, dr}{\int r^2 N(r)\, dr}, \tag{1}$$

where $N(r) = N_0 e^{-2\lambda r}$ is the exponential particle size distribution used in the GFDL microphysics scheme (S. J. Lin and L. Zhou 2019, unpublished manuscript). The intercept parameter is N_0 (m^{-4}), which equals to 8.0×10^6, 3.0×10^6, 4.0×10^6 for rain, snow, and graupel, respectively. The slope parameter is $\lambda = (\pi \rho N_0 / \rho_a q)^{1/4}$ (m^{-1}),

where ρ is the hydrometeor density, q is the hydrometeor mixing ratio, and ρ_a is the air density. The densities ($kg\,m^{-3}$) of rain, snow, and graupel are 1000.0, 100.0, and 400.0, respectively, which are consistent with the definitions in the CRTM. The effective radius defined in Eq. (1) represents the mean radius for scattering. Figure 1 shows the scatterplot of effective radius versus water content, and the histogram of effective radius for the precipitation species computed from all AMSU-A and ATMS observation locations over ocean of a single analysis. With the same amount of water content, snow has the largest effective radius, which is also more widely distributed.

The CRTM, version 2.3.0, has some enhancements for all-sky radiance assimilation. For example, the modeling of surface reflection under scattering condition has been improved by including reflection correction to remedy the missing diffuse radiation being reflected toward the viewing direction (Liu et al. 2015). Another upgrade in CRTM 2.3.0 enables the treatment of subgrid cloud and precipitation variability in radiative transfer with four cloud overlap schemes (van Delst et al. 2016). Since the goal of this study is to expand the all-sky radiance assimilation framework to include precipitating hydrometers, it would be better to evaluate this new framework based on the improved radiative transfer.

The implementation of the cloud overlap schemes in CRTM 2.3.0 is a two-column approach. The all-sky brightness temperature is the weighted average of the brightness temperature from the clear and the cloudy subcolumns of the grid box. The hydrometeor-weighted average cloud overlap scheme proposed by Geer et al. (2009) was utilized to compute the overall cloud fraction [Eq. (5) of Geer et al. 2009]. The cloud fraction of each layer was computed at each outer loop using the GFDL microphysics cloud fraction scheme.

The impact of upgrading the CRTM to version 2.3.0, as well as the impact of including the treatment of subgrid cloud variability using the average cloud overlap scheme are presented Fig. 2. Figure 2 compares the observation minus first guess (OmF) standard deviations and biases of simulations using CRTM 2.2.3 assuming overcast (CRTM2.2.3), CRTM 2.3.0 assuming overcast (CRTM2.3.0), and CRTM 2.3.0 with the average cloud overlap scheme (CRTM2.3.0avg). For all three simulations, the brightness temperatures were generated from the same first guess forecasts at C384 centered at synoptic times for a period from 10 to 20 July 2017. The OmF statistics were calculated for the observations over ocean in all-sky condition. The same observations that passed quality control in all three simulations were used in the comparison. The OmF
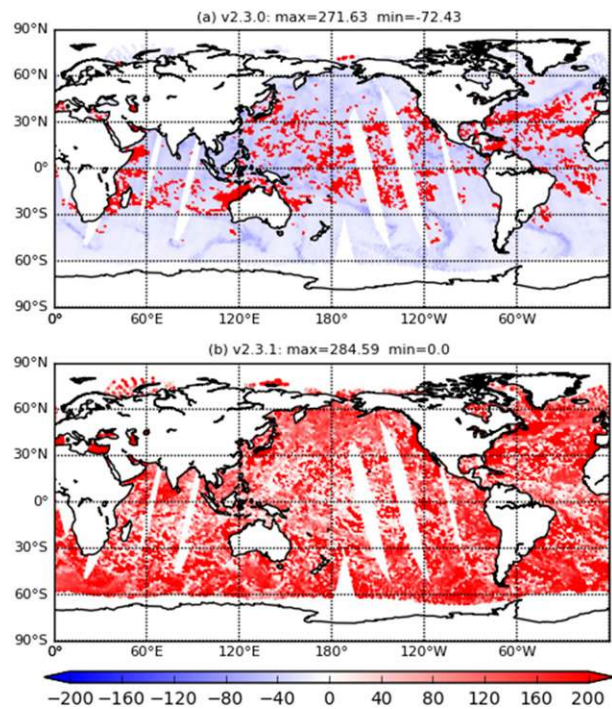

FIG. 3. Emissivity Jacobian (K) of AMSU-A (including *NOAA-15*, *NOAA-18*, *NOAA-19*, and *MetOp-A*) channel 2 calculated from the CRTM (a) before and (b) after the code error correction.

standard deviations of CRTM2.3.0 and CRTM2.3.0avg are normalized with respect to CRTM2.2.3. Negative normalized standard deviation means reduction of the standard deviation relative to CRTM2.2.3. The upgrade of CRTM to version 2.3.0 significantly reduces the positive biases of lower channels of AMSU-A (channels 1–4) and ATMS (channels 1–5) (Figs. 2b,d). It also reduces the OmF standard deviations of channels sensitive to hydrometeors. Including a cloud overlap scheme can further improve the simulated brightness temperature with even smaller OmF standard deviations. It largely reduces the negative OmF bias that might be overcorrected by CRTM 2.3.0 for AMSU-A channel 15. We also tested other cloud overlap schemes available in CRMT 2.3.0 and found that the average overlap scheme produced overall the best results. Therefore, the CRTM, version 2.3.0, with the average cloud overlap scheme was employed in the new all-sky radiance assimilation framework.

When initially running the new all-sky framework, it was found that the number of observations assimilated was significantly less than that in the original all-sky framework, although additional precipitation-affected radiances were supposed to be assimilated. Many more observations were rejected by surface emissivity sensitivity check, which was inherited from the original framework. Radiances from surface sensitivity channels
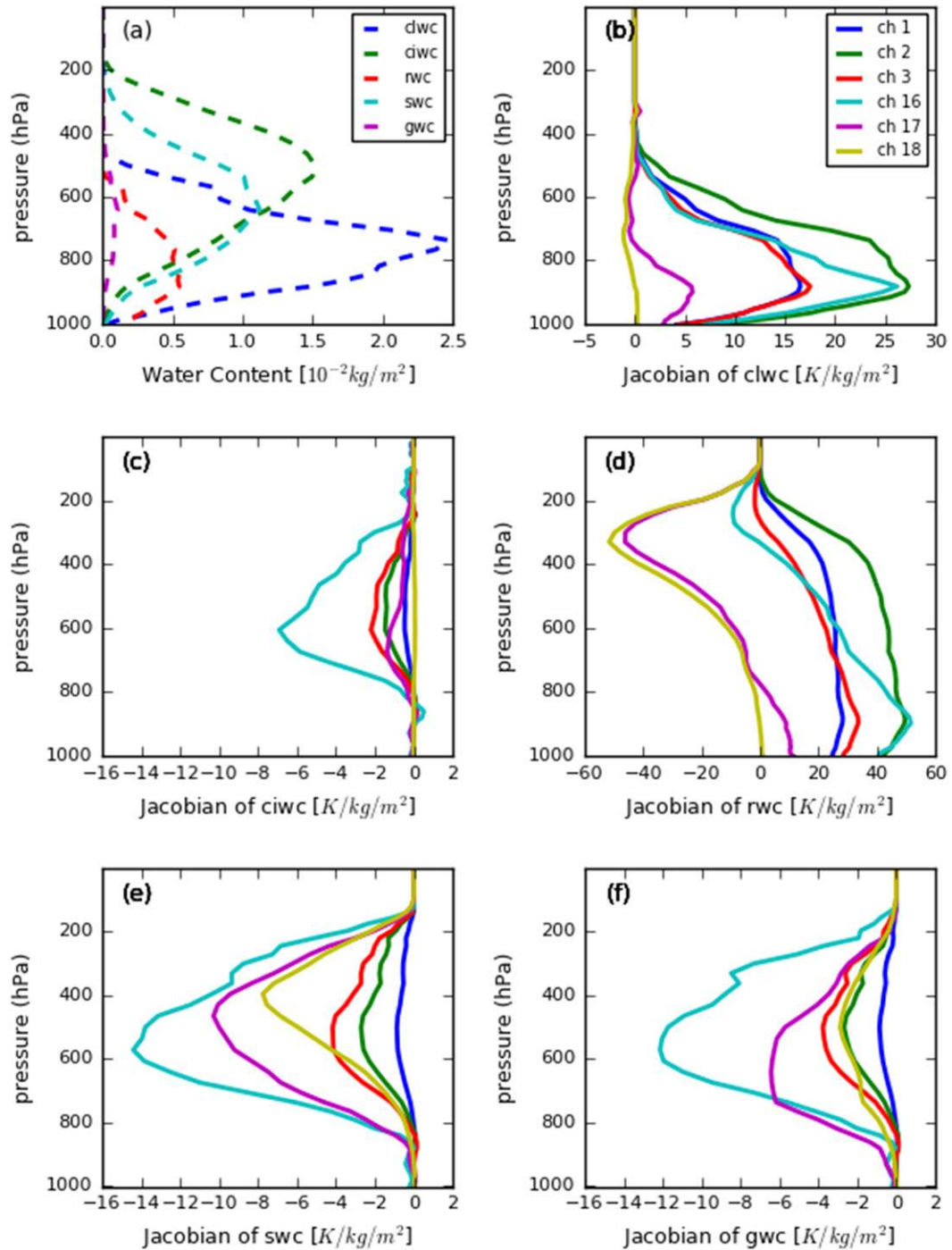
FIG. 4. (a) Mean vertical profiles of the hydrometeors and mean Jacobians of (b) cloud liquid water (clwc), (c) cloud ice (ciwc), (d) rain (rwc), (e) snow (swc), and (f) graupel (gwc) for ATMS channels 1, 2, 3, 16, 17, and 18. The profiles are averaged over locations with precipitation water path larger than 0.01 kg m^{-2}.

are excluded, when the ratio between OmF and surface emissivity Jacobian is larger than an empirical threshold. This quality control is more critical for observations over land, and it is relaxed, where cloud liquid water

path retrieved from observed brightness temperature is larger than 0.1 kg m^{-2} (Zhu et al. 2016, 2019). The surface emissivity Jacobians produced by the CRTM under scattering condition contains a lot of small negative
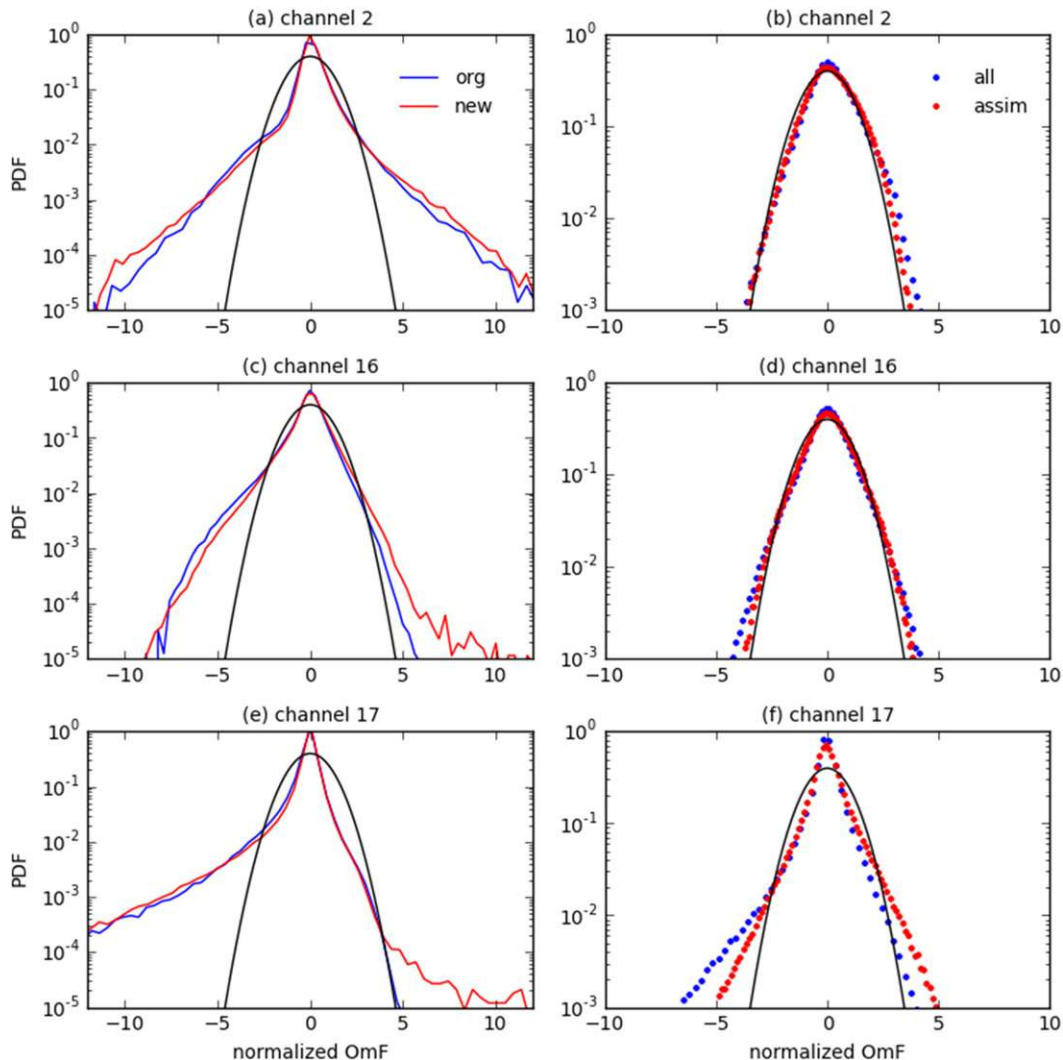
FIG. 5. Histograms of OmF for the period of July 2017 from ATMS (a),(b) channel 2 (31.4v GHz); (c),(d) channel 16 (88.2v GHz); and (e),(f) channel 17 (165.5h GHz). (left) OmF of all observations normalized by the data sample standard deviation in the original all-sky framework (org, blue) and in the new all-sky framework (new, red). (right) OmF of all (blue) and assimilated (red) observations normalized by the symmetric observation errors in the new framework. Gaussian distribution is shown as the black curves.

values in surface-sensitive channels (e.g., AMSU-A channel 2 in Fig. 3a). The negative surface emissivity Jacobians are not physically meaningful because larger surface emissivity should produce higher brightness temperature. The problem was caused by a CRTM code error. Surface emissivity Jacobians for surface-sensitive channels became all positive (Fig. 3b), after the error was corrected. Besides quality control, surface emissivity Jacobian is also used in observation error inflation, and it is a bias correction predictor. Therefore, the fix is essential if precipitation-affected radiances are assimilated using the CRTM. The correction of the code error will be included in the next CRTM release and it is also documented in Liu et al. (2019).

To help understand the impact of the hydrometeors on the OmF statistics in later discussion, the CRTM calculated brightness temperature Jacobians with regard to the hydrometeors are presented in Fig. 4. Figure 4 shows the mean vertical profiles of the hydrometeors and the mean Jacobians for selected ATMS channels in the presence of precipitation. All the selected channels, except for channel 18, show positive sensitivity to cloud liquid water and negative sensitivity to cloud ice (Figs. 4b,c). Channel 18 shows almost no sensitivity to cloud ice and very small negative sensitivity to cloud liquid water in the middle troposphere. The brightness temperature Jacobians for rain have positive values in lower-frequency channels (channels 1, 2,

and 3), and have negative peaks above the top of the rain layer in higher-frequency channels (channels 16, 17, and 18). All these channels show negative sensitivities to both snow and graupel due to their scattering effects (Figs. 4e,f). Channels 16 and 17 have larger sensitivities to snow and graupel than other channels.

b. Observation error

The observation errors were estimated based on the symmetric cloud amount (Geer and Bauer 2011; Geer et al. 2012). The symmetric cloud amount is defined as

$$\overline{\text{CLW}} = \frac{\text{CLW}_{\text{FG}} + \text{CLW}_{\text{OBS}}}{2}, \qquad (2)$$

where CLW_{FG} and CLW_{OBS} are the retrieved cloud liquid water (kg m^{-2}) computed from the first guess and observed brightness temperature using the retrieval formula of Grody et al. (2001) and Weng et al. (2003) [see Eq. (1) of Zhu et al. 2016]. The symmetric observation errors were estimated by linear fitting the standard deviations of OmF binned by $\overline{\text{CLW}}$.

The left panels of Fig. 5 compare the histograms of OmF from selected ATMS channels that cover low, middle, and high frequencies in the original (blue) and the new (red) all-sky frameworks. The data sample contains OmF of all observations passed data thinning without applying any quality control. The OmF normalized by the standard deviation of the data sample shows similar non-Gaussian characteristics in both the original and the new all-sky frameworks. The OmF distributions are right skewed in channel 2 and become more left skewed in higher-frequency channels. The new framework slightly reduces the negative skewness of channel 16. The data sample in the new framework contains more large FG departures. The symmetric observation errors defined in Table 1 of Zhu et al. (2016) for AMSU-A channels and in Table 3 of Zhu et al. (2019) for ATMS channels are generally valid in the current configuration of the new framework and are used in this study. Although the standard deviations of OmF in the new framework are larger, the original symmetric observation errors were inflated for most of the channels sensitive to hydrometeors, and observations with large FG departures were excluded by quality control. The right panels of Fig. 5 show the histogram of OmF normalized by those symmetric observation errors for all observations (blue) and assimilated observations (red). The symmetric observation error normalized OmF distributions are closer to Gaussian distribution, especially for assimilated observations.

The situation dependent observation error inflation employed in Zhu et al. (2016) was also used in this study.
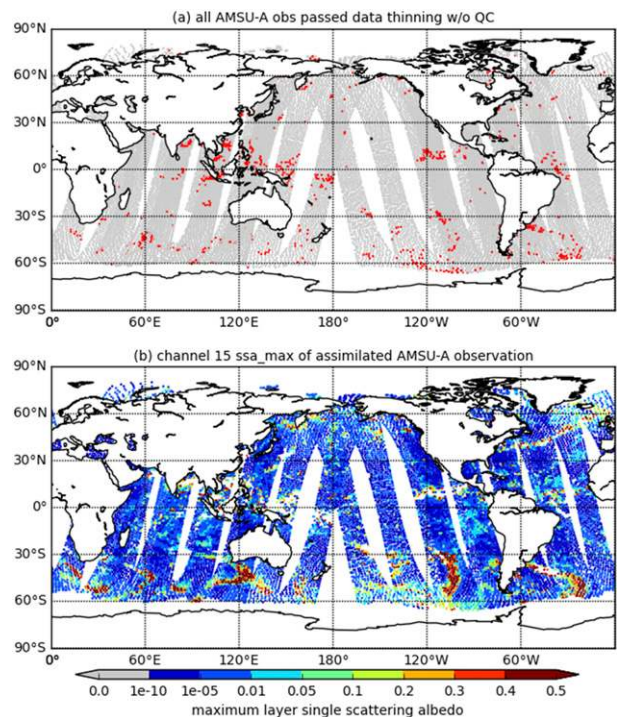

FIG. 6. (a) Locations of all AMSU-A observations (including *NOAA-15*, *NOAA-18*, *NOAA-19*, and *MetOp-A*) that passed data thinning without quality control being applied at 0000 UTC 15 Jul 2017. Observations that meet the precipitation screening criterion are shown in red. These observations are rejected in the original all-sky framework but are kept for potential assimilation in the new all-sky framework. (b) AMSU-A channel 15 maximum layer single-scattering albedo of assimilated observations in the new all-sky framework.

The additional inflations based on a few physical factors aim to moderate the impact of observations with large FG departures. The final observation error variance is the sum of the symmetric observation error variance and the variances of the inflated errors (Zhu et al. 2016). The situation dependent observation error inflation made additional 20%–40% reduction in the standard deviations of the normalized OmF in channels sensitivity to hydrometeors.

c. Quality control

Precipitation screening used in the original all-sky framework was removed in the new framework, so that precipitation-affected radiances can be restored for assimilation. Figure 6a shows all the AMSU-A observations passed data thinning before quality control being applied in a single cycle example. The observations in red are detected as precipitation-affected radiances based on the empirical formula of Eqs. (4) and (5) in Zhu et al. (2016). These observations are the additional radiances restored for assimilation in

TABLE 1. List of experiments.

Experiment	Control variable	CRTM	Precipitation screening	Update hydrometeors
CNTL	Cloud water	2.2.3	Yes	No
QLQI	Cloud liquid water and cloud ice	2.2.3	Yes	No
ALLQ	Cloud liquid water, cloud ice, rain, snow, and graupel	2.3.0 with averaged cloud overlap scheme	No	No
ALLQ_cycle_hydro	Cloud liquid water, cloud ice, rain, snow, and graupel	2.3.0 with averaged cloud overlap scheme	No	Yes

the new framework but are excluded in the original framework.

It will be shown later that the FG departures have large biases in deep-convection regions. The quality control based on the cloud effect of channel 5/6 for AMSU-A/ATMS (Geer et al. 2012; Zhu et al. 2016, 2019) was retained to screen out observations in deep-convection regions.

The cloud effect is defined as the difference between all-sky brightness temperature (observed or simulated) and simulated clear-sky brightness temperature. To avoid biases caused by asymmetric sampling (Geer et al. 2012), both observed and simulated cloud effect were used to screen out observations in the new framework when either of them is less than -0.5 K.
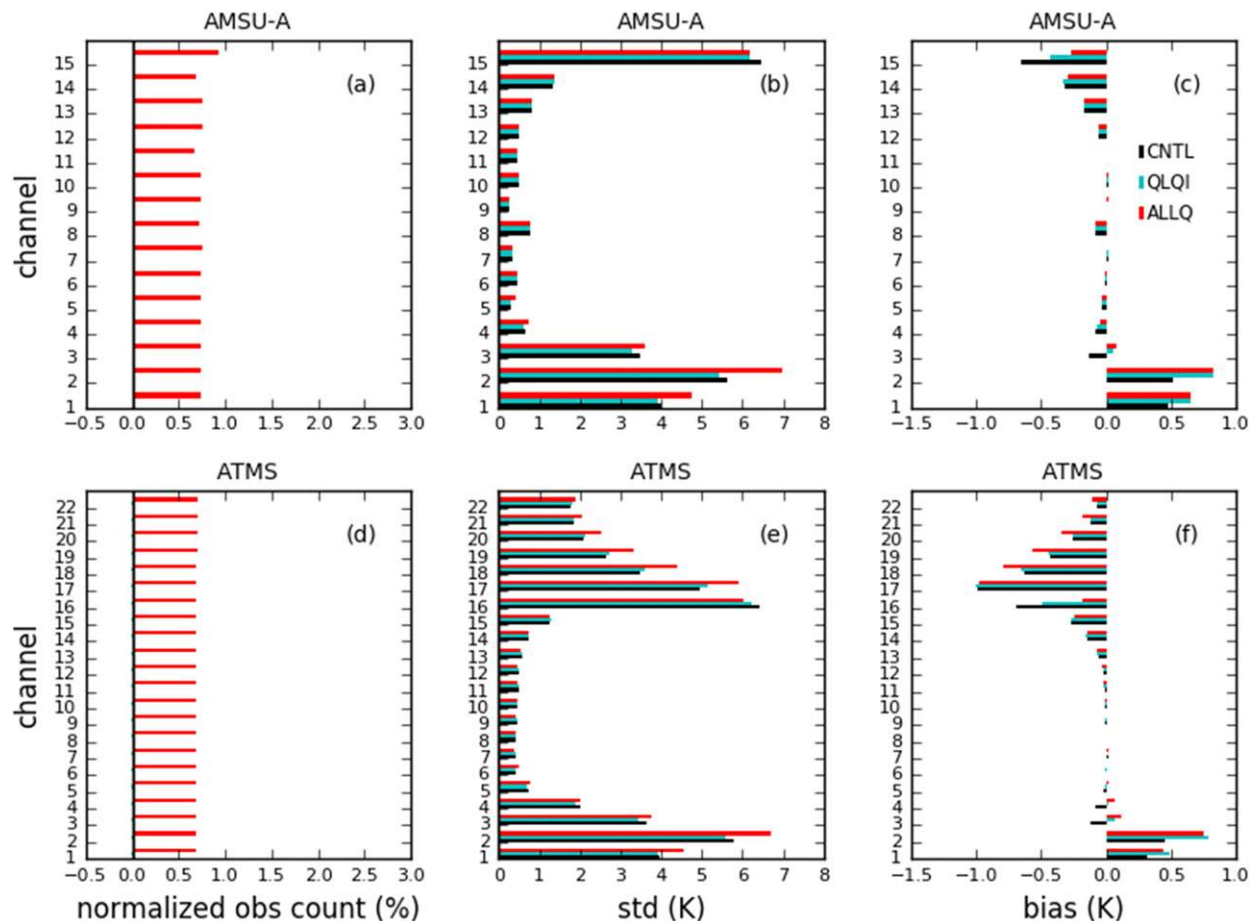

FIG. 7. (a),(d) Normalized differences of observation counts; (b),(e) OmF standard deviations; and (c),(f) OmF biases of (top) AMSU-A (including *NOAA-15*, *NOAA-18*, *NOAA-19*, and *MetOp-A*) channels and (bottom) ATMS (*SNPP*) channels for the period from 1 Jul to 31 Aug 2017. The observation counts of the QLQI and ALLQ are normalized by the CNTL values. The statistics are for all the observations over ocean that passed data thinning without quality control being applied. The OmF statistics are computed after bias correction.
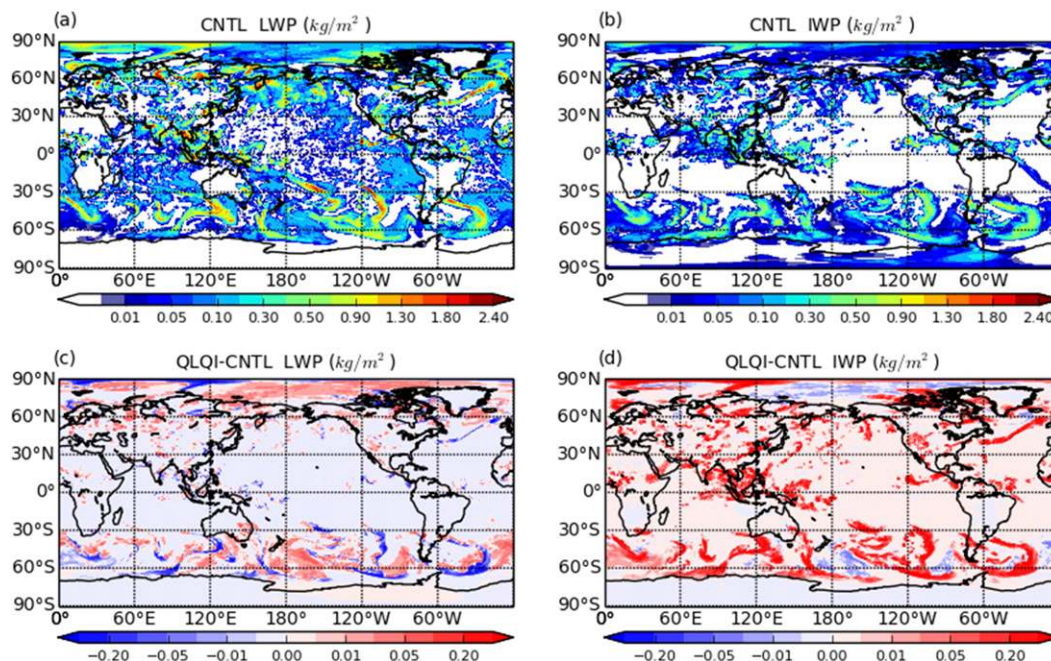
FIG. 8. (a) Cloud LWP (kg m^{-2}) and (b) cloud IWP (kg m^{-2}) of the CNTL and the differences of (c) LWP and (d) IWP between the CNTL and the QLQI (QLQI − CNTL) at 0000 UTC 15 Jul 2017.

The gross error check in the original all-sky framework is based on the OmF normalized by the final observation error (Zhu et al. 2016, 2019). The final observation error involves various situation dependent error inflation, especially for observations assimilated in all-sky approach. In this new framework, we tightened the gross error check by using the symmetric observation error normalized OmF to screen out observations, when it is greater than 2.5. By examining the extra observations screened out by the modified gross error check, we found that most of the observations indicated large disagreement with the FG in terms of cloud location and cloud amount. The attempt was to exclude the observations with very large OmF and mismatched cloud information instead of inflating their observation errors. The latter can contribute to the non-Gaussianity of the normalized OmF (e.g., Fig. 6 of Zhu et al. 2016). Excluding those observations may also reduce model shocks due to large differences in cloud location and cloud amount between FG and observations.

The assimilated AMSU-A channel 15 observations in the new framework are shown in Fig. 6b. Comparing to Fig. 6a, the blank areas in Fig. 6b are observations tossed by quality control, which mainly rejected observations in deep-convection regions. The quantity shown in Fig. 6b is the maximum single-scattering albedo of the vertical layers computed in the CRTM. The threshold of 10^{-10} is used to determine whether scattering radiative transfer will be turned on in the CRTM. In high-frequency

channels like channel 15, the maximum single-scattering albedo in all assimilated observation locations are greater than 10^{-10}. Therefore, scattering radiative transfer is activated in all those observation locations. In lower-frequency channels, such as AMSU-A channels 1 and 2, which are less sensitive to scattering, about 75% of the assimilated observations are simulated with multiple scattering turned on (not shown). In the CRTM, nonprecipitating hydrometeors (cloud liquid water and cloud ice) are assumed to be very small particles comparing to the microwave wavelengths, and their scattering effects are ignored with their single-scattering albedos hardcoded to be zero. Without precipitating hydrometeors present in the original all-sky framework, radiative transfer is always solved in emission mode. Although some of the restored precipitation-affected radiances were excluded by other QC procedures in the new framework, they are a small part of the observations where significant scattering was detected in the model forecast (Fig. 6b).

4. All-sky radiance assimilation experiments and results

a. Experiments

Four experiments (Table 1) were conducted to evaluate the performance of this upgraded all-sky radiance assimilation framework. The control experiment (CNTL) utilized the original all-sky radiance assimilation framework
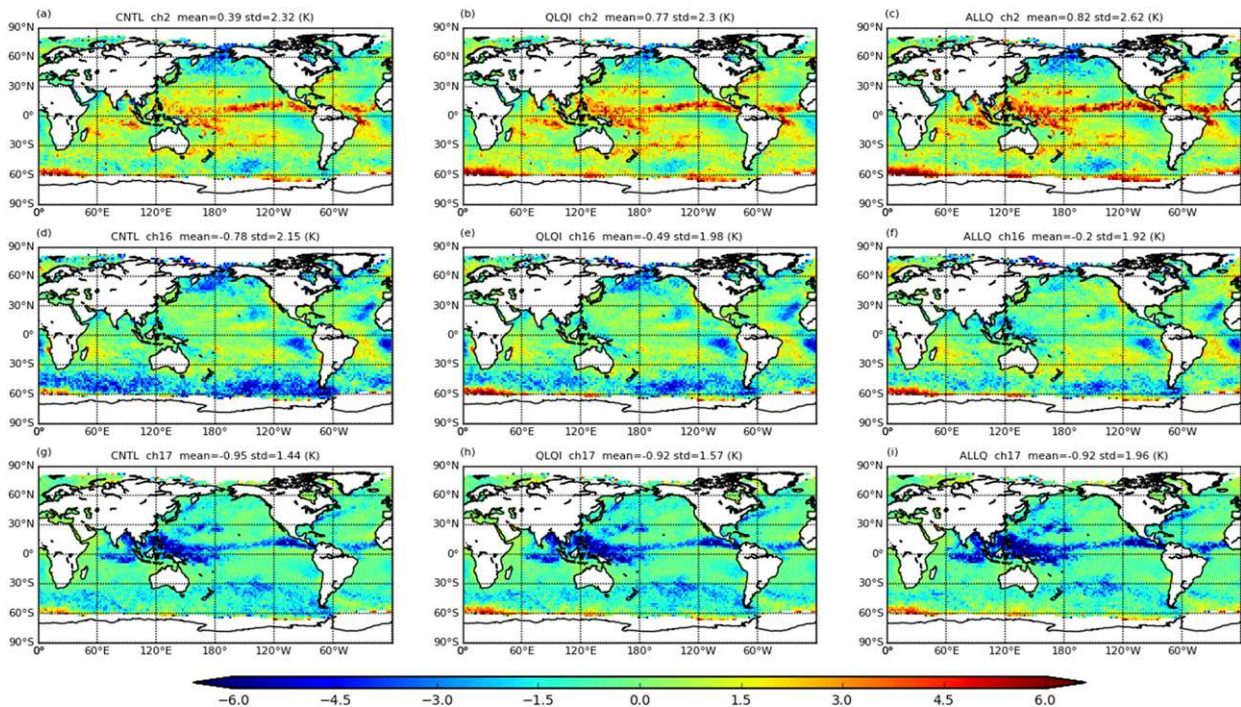
FIG. 9. One-month averaged OmF (K) distributions of July 2017. The OmFs are from all observations over ocean without quality control being applied. (a)–(c) ATMS channel 2 (31.4v GHz), (d)–(f) channel 16 (88.2v GHz), and (g)–(i) channel 17 (165.5h GHz). Experiments compared are (left) CNTL, (center) QLQI, and (right) ALLQ.

adopted for the FY19 FV3GFS, in which the normalized CW was the cloud control variable. We conducted an intermediate experiment QLQI to understand the effects of the cloud decomposition. The QLQI experiment was identical to the CNTL, except that the normalized Ql and Qi were the cloud control variables. Two other experiments, ALLQ and ALLQ_cycle_hydro, were based on the new all-sky radiance assimilation framework, in which the model state variables and cloud control variables were expanded to include precipitating hydrometeors. The analysis increments of the hydrometeors were used to update the model state for the forecast in the ALLQ_cycle_hydro experiment but were not in the ALLQ experiment.

All the experiments utilized the same cold-start initial condition from the operational GSM GFS for both the control and ensemble. The experiments were run at a reduced horizontal resolution of C384 (~25 km) for the control and C192 (~50 km) for the ensemble. The experiment period is from 16 June 2017 to 31 August 2017. Variational bias correction coefficients were spun up from zero in all the experiments.

b. Data usage and FG departure statistics

The characteristics of the FG departure and data usage are evaluated for CNTL, QLQI, and ALLQ experiments

in this section. Figure 7 compares the data counts and OmF statistics of all the AMSU-A and ATMS observations passed data thinning for the three experiments using different cloud control variables. Quality control is not applied for the data sample shown in Fig. 7. For both AMSU-A and ATMS channels, only radiance over ocean are assimilated in all-sky approach. Therefore, the statistics compared here are from radiances over ocean. Figures 7a and 7d show that there is little difference between the CNTL and the QLQI in the number of observations passed data thinning, which is expected because the data thinning procedures in the two experiments are identical and precipitation screening was applied in both experiments. The 0.7%–0.9% increases of observations in the ALLQ experiment is mainly due to the removal of the precipitation screening in the data thinning procedure. The data thinning does not distinguish channels at the same observation location. When precipitation screening is relaxed, all channels at a certain observation location can be restored for potential assimilation. Therefore, the observations passed data thinning are uniformly increased over all the channels in the ALLQ experiment. The CNTL and the QLQI experiments have different OmF statistics because cloud liquid water and cloud ice are partitioned from cloud water in the CNTL, whereas cloud liquid water and
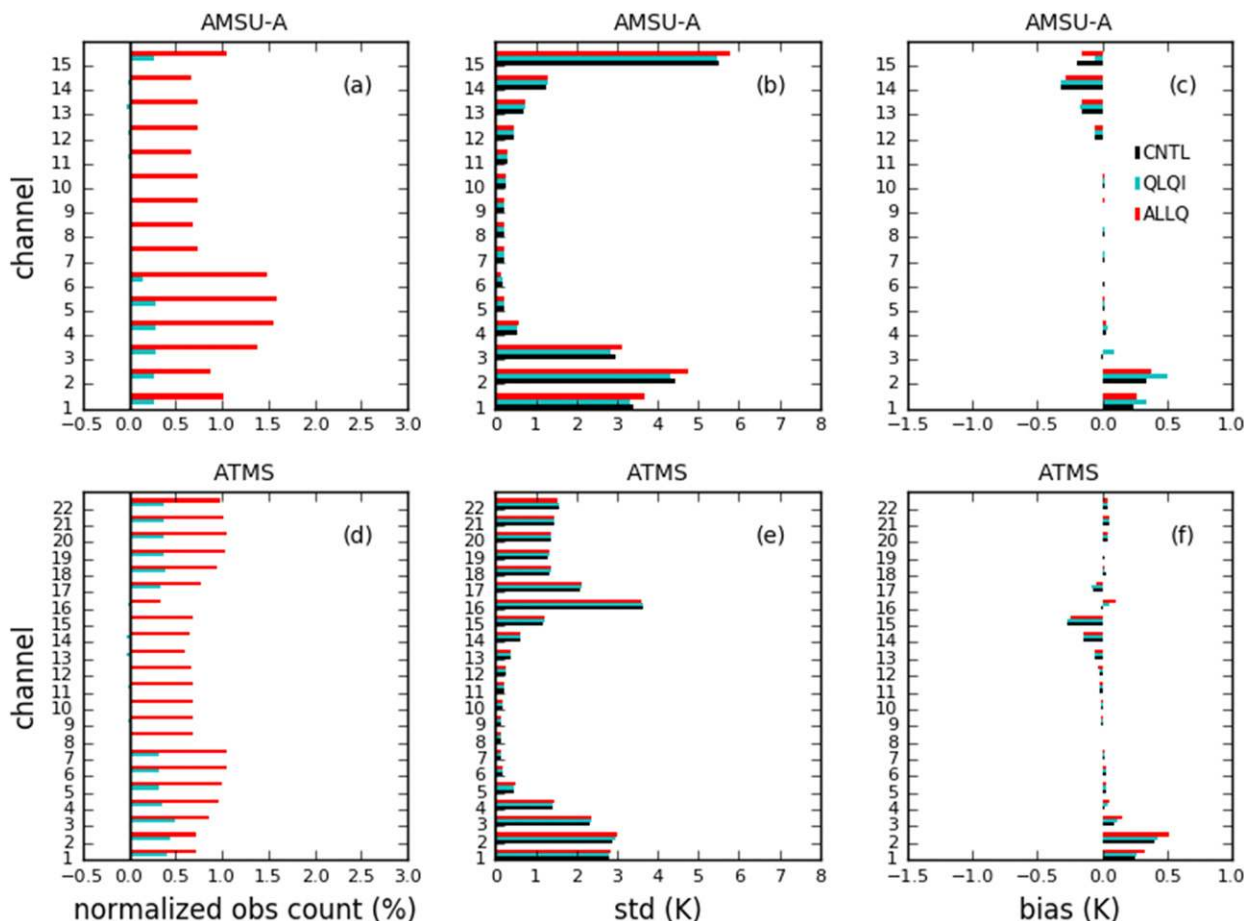
FIG. 10. As in Fig. 7, but for assimilated observations over ocean.

cloud ice directly come from the model forecast in the QLQI experiment. Without using the empirical decomposition, QLQI has smaller OmF standard deviations in the imaging channels and lower troposphere temperature sounding channels for both AMSU-A (channels 1–4 and 15) and ATMS (channels 1–5 and 16) (Figs. 7b,e). The QLQI has larger positive biases in channels 1 and 2 of both AMSU-A and ATMS, and smaller negative bias in channel 15/16 of AMSU-A/ATMS comparing with the CNTL (Figs. 7c,f). This indicates that the QLQI FG brightness temperature is generally colder than that of the CNTL in those cloud-sensitive channels. The FG cloud liquid water path (LWP) and cloud ice water path (IWP) of a single simulation using the setups of the two experiments are compared in Fig. 8. The QLQI generally has less cloud liquid water and more cloud ice than the CNTL, especially, in areas with thick clouds. In the CRTM, decreasing cloud liquid water and increasing cloud ice reduce brightness temperature due to their positive and negative Jacobians for those channels as shown in Figs. 4b and 4c. Therefore,

the QLQI tends to have colder simulated brightness temperature than the CNTL.

When precipitating hydrometeors are present in the ALLQ experiment, the OmF standard deviations are larger than the CNTL in channels sensitive to hydrometeors, except for channel 15/16 of AMSU-A/ATMS. The ALLQ experiment has larger positive bias in imaging channels 1 and 2 for both AMSU-A and ATMS, and larger negative biases in moisture sounding channels 18–22 of ATMS. The model may have larger error in predicting the location and intensity of precipitation. The optical properties of the precipitating hydrometeors, particularly, the scattering properties for snow and graupel, may also be modeled inaccurately in the CRTM. These two sources of errors can both contribute to the larger OmF standard deviations and biases when precipitating hydrometeors are included.

The spatial distributions of the one-month averaged OmF from the three experiments are compared in Fig. 9. Channels 2 (31.4 GHz), 16 (88.2 GHz), and 17 (165.5 GHz) of ATMS, which are most representative of the OmF
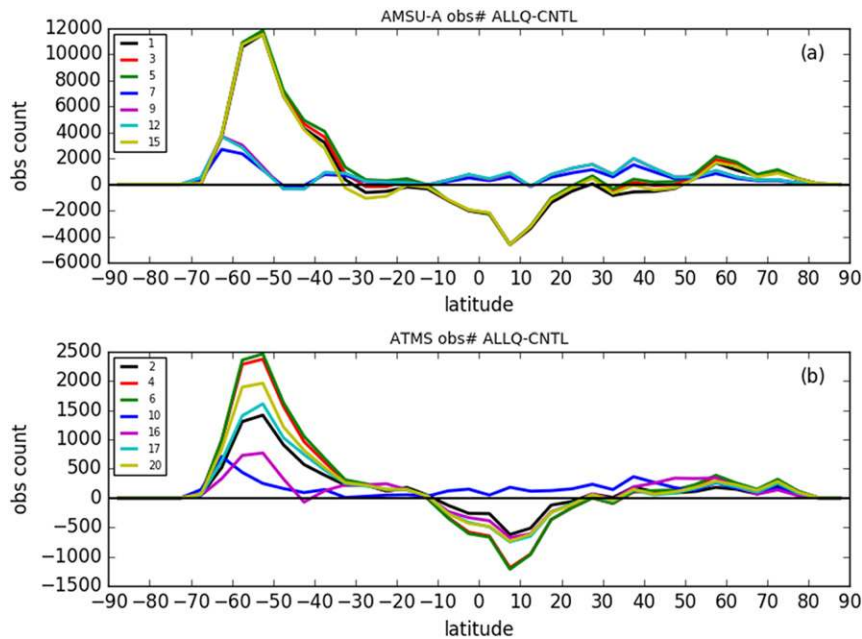
FIG. 11. Latitudinal differences of assimilated number of observations over ocean between the ALLQ and the CNTL for selected (a) AMSU-A and (b) ATMS channels. The differences are computed as the number of observations assimilated in the ALLQ minus that of the CNTL over the period of July 2017.

differences among the experiments, are selected. The characteristics of the OmF distributions in AMSU-A equivalent channels are similar. The positive bias in ATMS channel 2 is mainly located in the intertropical convergence zone (ITCZ) and in high-latitude areas in the Southern Hemisphere. This may be caused by the lack of clouds in those areas. Fewer liquid clouds and more ice clouds can also contribute to the larger positive bias as can be seen by comparing the QLQI with the CNTL in Figs. 9a and 9b. Adding rain can reduce the positive bias because of the positive Jacobian of rain in channel 2 (Fig. 4d), but this is offset by the scattering effects from snow and graupel in the ALLQ experiment (Fig. 9c). In higher-frequency channels, the FG departures are dominated by negative values. At 88.2 GHz, the negative OmF biases in the CNTL (Fig. 9d) can be reduced, when cloud liquid water and cloud ice input to the CRTM are directly from the model output in the QLQI (Fig. 9e), and can be further reduced by introducing precipitating hydrometeors (Fig. 9f). At 165.5 GHz, the ALLQ OmF in the ITCZ shows larger negative values (darker blue). In the ITCZ, the FG brightness temperature is already too warm in the 165 GHz channel in the QLQI. Including precipitating hydrometeors makes it even warmer in the ALLQ. In tropical deep-convection regions, the colder bias appears in all high-frequency humidity sounding channels 17–22 (Fig. 7f). This may indicate that the scattering

properties of frozen hydrometeors are not optimal in the CRTM LUTs. The scattering produced by the frozen hydrometeors may not be enough in high-frequency channels. The similar scene has been shown as a result of representing snow as Mie sphere in Geer and Baordo (2014). Improving scattering properties of frozen hydrometeors is another major effort. We will investigate more on this in the future.

The data counts and OmF statistics of assimilated observations over ocean are compared for the three experiments in Fig. 10. Slightly more observations are assimilated in the QLQI experiment than in the CNTL. By checking the number of observations excluded by different QC procedures, it was found that more observations were rejected in the CNTL due to larger absolution value of OmF. Here we would like to focus more on the ALLQ experiment. The number of assimilated observations further increases in the ALLQ. Figure 11 shows that the increase in the number of assimilated observations is largely in the Southern Hemisphere (SH). The increase in observation count in the Northern Hemisphere (NH) is small because the NH has more land coverage and much less precipitation-affected radiances are detected (Fig. 6a). For channels sensitive to hydrometeors, the number of assimilated observations reduces in the tropics. As we have seen from Fig. 9 that the OmFs in the ALLQ are larger in the tropical deep-convection region, therefore,
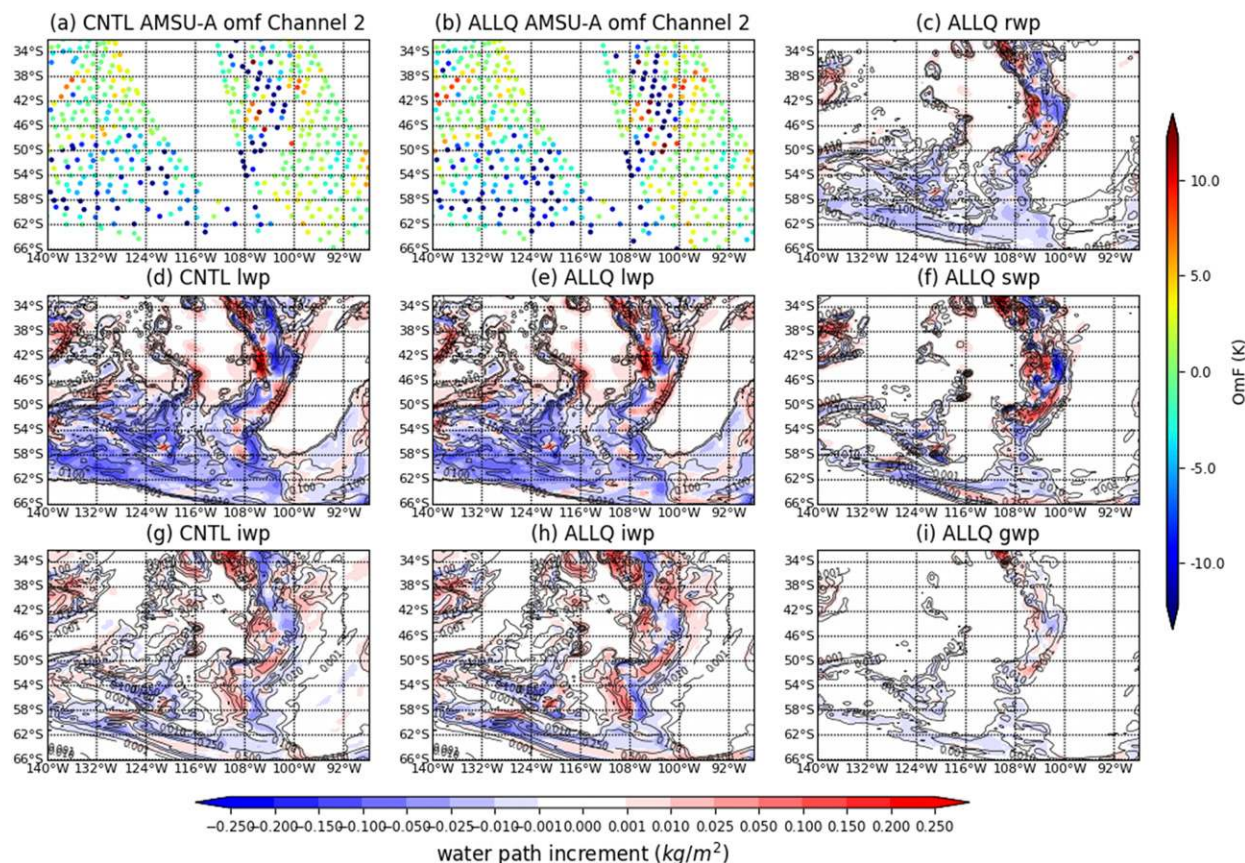
FIG. 12. OmF of assimilated AMSU-A channel 2 observations in (a) the original (CNTL) and (b) the new framework (ALLQ) from a single cycle analysis that only assimilate AMSU-A all-sky radiances with the same first guess centered at 0000 UTC 15 Jul 2017. Other panels are the first guess (black contours) and analysis increment (color shades) valid at $t + 1$ h (0100 UTC) of the assimilation window of cloud liquid (lwp) and cloud ice (iwp) water path (kg m^{-2}) in (d),(g) the CNTL and (e),(h) the ALLQ; and of (c) rain, (f) snow, and (i) graupel water path (kg m^{-2}) in the ALLQ. The OmF shown in (a) and (b) are within a 1-h window centered at 0100 UTC.

more observations in the tropics are excluded. The percentage of increase in observation count is small in the ALLQ because only a small fraction of the observations (3.5% and 2.6% for AMSU-A and ATMS, respectively) are detected as precipitation, and most of them are located in deep-convection regions (Fig. 6a). The presence of precipitation in the FG, which triggers the scattering radiative transfer (Fig. 6b), is the main contributor to the differences in OmF between the new and the old framework.

The OmF of the ALLQ is closer to the OmF of the CNTL after QC (Fig. 9) with slightly larger standard deviations and biases in some of the channels. In general, the simulated brightness temperature in the ALLQ is colder than that in the CNTL due to the scattering effect of the newly introduced frozen hydrometeors, and to some extent the differences in the distribution of cloud liquid water and cloud ice as a result of the cloud decomposition in the CNTL.

c. Impact on analysis

To understand the impact of cloud and precipitation-affected radiances on the analysis of model fields, we conducted two single cycle experiments with only AMSU-A all-sky radiances assimilated using the original (CNTL) and the new all-sky framework (ALLQ). The same first guess coming from the cycled CNTL experiment was used in both experiments. Figure 12 compares the OmF of assimilated AMSU-A channel 2 radiances and analysis increments of hydrometeors in the two experiments. The north–south-oriented cloud and precipitation between 108° and 100°W is associated with a front between a low pressure system and a high pressure system in the Southern Hemisphere (Fig. 13a). Cloud and precipitation also appear in the low pressure system and in the area, where the winds from the two pressure systems converge with polar winds. Note, there are some observations shown in the ALLQ (Fig. 12b)
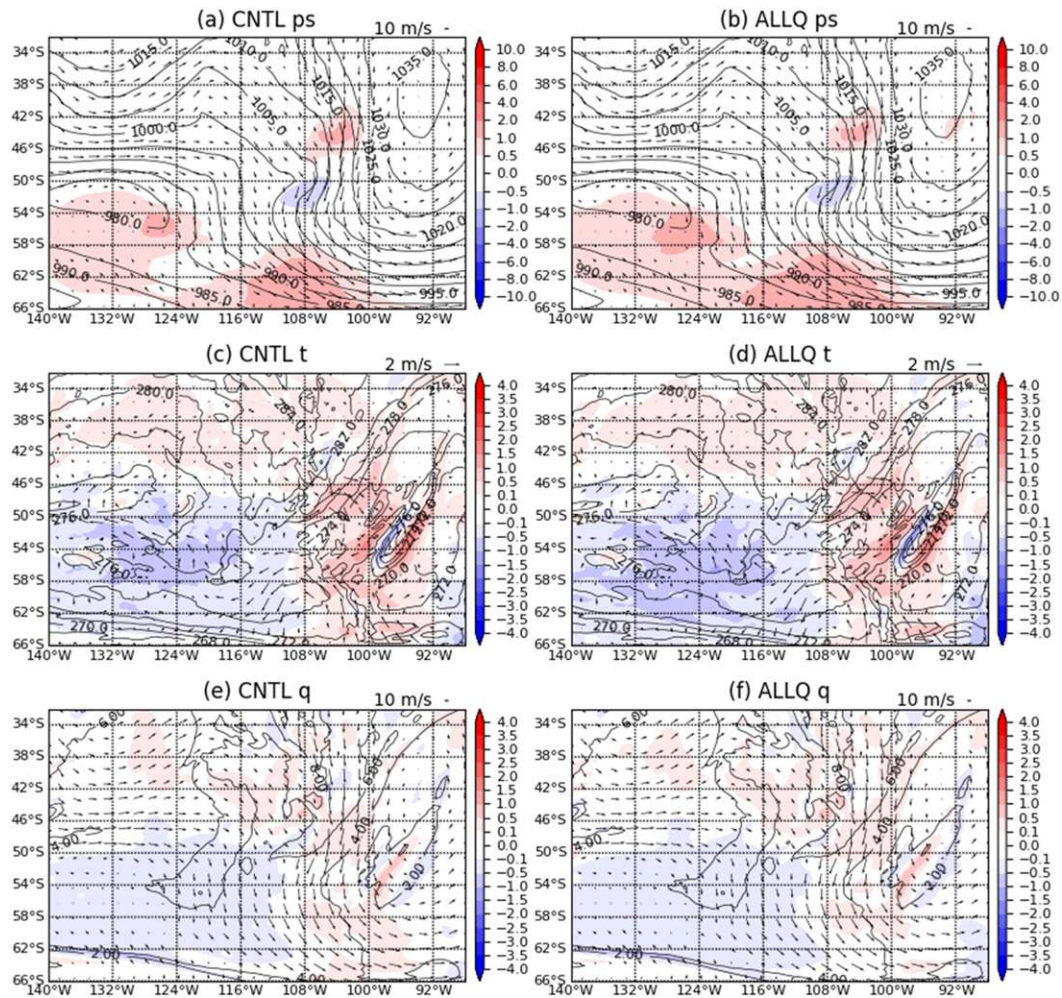
FIG. 13. First guess and analysis increment of (a),(b) surface pressure (hPa); (c),(d) temperature (K); and (e),(f) specific humidity (g kg^{-1}) in the (left) CNTL and (right) ALLQ from the same single cycle analysis in Fig. 12. The wind vectors are first guess in (a) and (b), analysis increment in (c) and (d), and analysis in (e) and (f).

but not in the CNTL (Fig. 12a). For example, in the area over 42°–54°S and 108°–100°W, the extra observations assimilated in the ALLQ are detected as precipitation-affected radiances, and they are located right in the area covered by rain, snow, and graupel in Figs. 12c, 12f, and 12i. While those observations were rejected by precipitation screening in the original framework as shown in the CNTL (Fig. 12a). The analysis increments of cloud liquid water and cloud ice look similar between the two experiments, except slight difference in the magnitude of the increments. Some minor differences can also be found in areas, where observations are absent in the CNTL experiment. Generally speaking, the amount of cloud and precipitation reduces where OmF is negative and increases where OmF is positive, although the increments of different hydrometeors do not always show the same sign in the same location due to their different

sensitivities (Fig. 4). For this particular case, the amount of cloud and precipitation reduces in most of the areas shown in Fig. 12, which indicates a weaker system. The peak value of the precipitation in the frontal cloud is reduced or shifted in the ALLQ experiment (Figs. 12c,f,i).

Figure 13 shows that the adjustments in mass and wind fields in the cloudy area are consistent with the changes in the hydrometeors in both experiments. The low pressure system is weakened (Figs. 13a,b) accompanied with anticyclonic wind increments (Figs. 13c,d). The positive surface pressure increment near the frontal cloud reflects the reduction of cloud and precipitation near that area. Negative temperature and moisture increments can be found where the amount cloud and precipitation are reduced. The increments of mass, wind and moisture fields are similar in the two experiments,
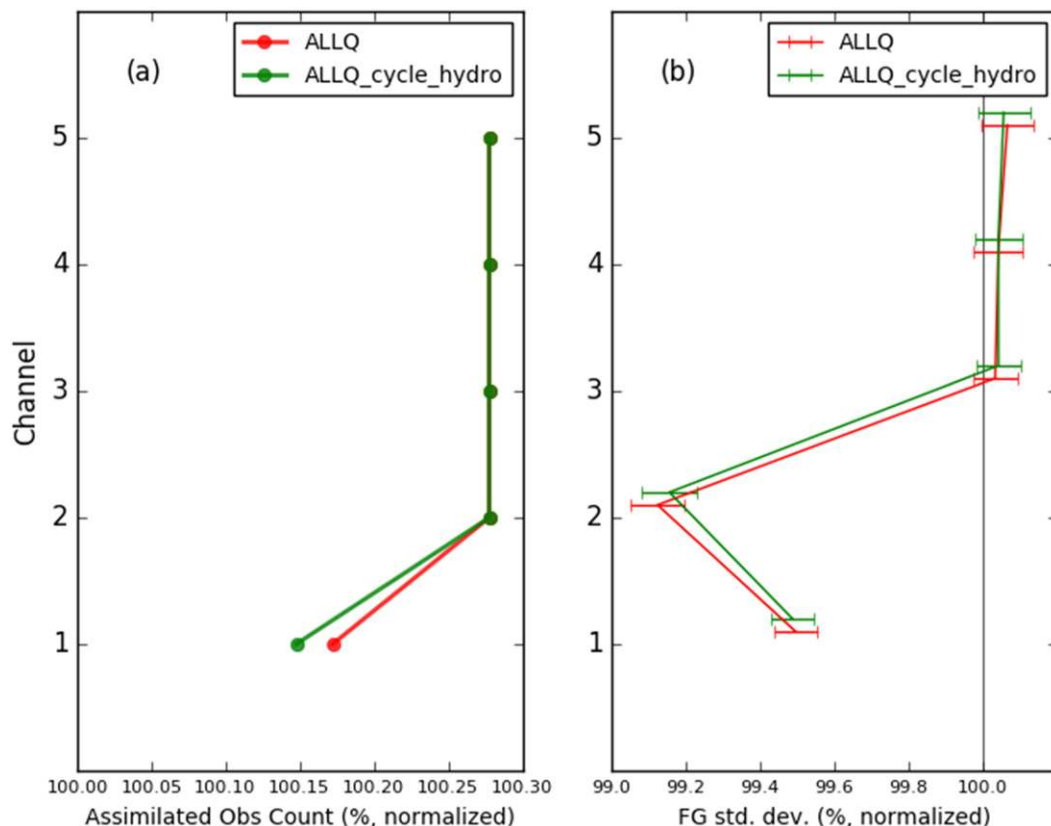
FIG. 14. Normalized differences of (a) mean assimilated observation counts and (b) OmF standard deviation of bias-corrected MHS (including *NOAA-18*, *NOAA-19*, *MetOp-A*, and *MetOp-B*) observations. The normalization was performed against the CNTL. The error bars indicate the 95% confidence interval.

except that the magnitudes of the increments are slightly large in the ALLQ experiment, which reflects the impact from the additional precipitating hydrometeors.

In the cycled experiments (not shown), negative zonal mean cloud and precipitation increments can be found between 60° and 40°S. Hydrometeor increments are all positive in the tropics. The new framework contains slightly more cloud liquid water in the analysis. In the comparison of the mean temperature and relative humidity analyses against ECWMF's analysis, only minor differences were found between the original and the new framework. The temperature analysis of the new framework matches ECWMF's analysis significantly better below 600 hPa in terms of RMS difference.

d. Impact on forecast skills

The forecast performance of this upgraded all-sky assimilation framework is evaluated based on the two and a half months fully cycled CNTL, ALLQ, and ALLQ_cycle_hydro experiments. The ALLQ_cycle_hydro is used to evaluate the impact of cycling the hydrometeors (without zeroing out analysis increments of

the hydrometeors) in the system. The late data cutoff (GDAS) analysis (Kleist et al. 2009a) were fully cycled for all the experiments. The early data cutoff (GFS) analysis and subsequent 10-day free forecast were only run for the 0000 UTC cycle. The first 10 days of the results were disregarded to account for system spinup.

To evaluate the impact on short-range forecast, the FG fits to other observations were examined. Figure 14 shows assimilated data counts and the fit to the Microwave Humidity Sounder (MHS) observations. More MHS observations were assimilated in both experiments with precipitating hydrometeors included. The reductions of the OmF standard deviations of channel 1 and 2 are quite significant. Although the impact on the OmF standard deviations in channels 3–5 is neutral, the number of assimilated observations increased. Generally speaking, the FG fit to the MHS observations is improved. The FG fits to in situ wind observations, atmospheric motion vector (AMV) and Global Positioning System Radio Occultation (GPS-RO) observations were also evaluated. The results are mostly neutral (not shown). The improvement in the fit to AMV between 400 and 300 hPa is
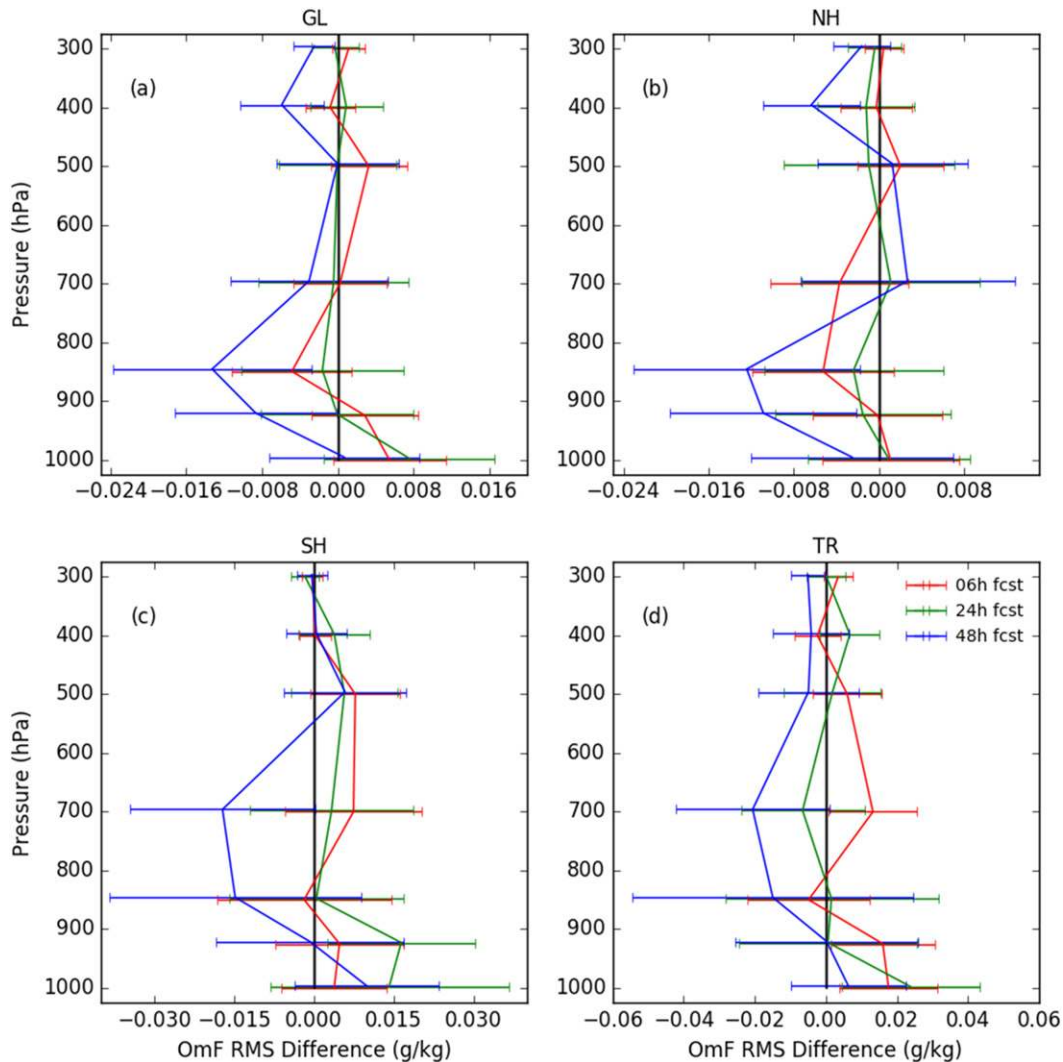
FIG. 15. The change of forecast fit (RMS of observation minus forecast) to radiosonde specific humidity observations (g kg^{-1}) of the ALLQ with respect to (a) the CNTL globally, (b) in the Northern Hemisphere, (c) the Southern Hemisphere, and (d) the tropics.

significant in both ALLQ and ALLQ_cycle_hydro experiments and more AMV observation were assimilated between 400 and 250 hPa.

Figure 15 shows the differences of the 6-, 24-, and 48 h-forecast fits to radiosonde (raob) specific humidity observations of the ALLQ experiment with respect to the CNTL. Globally, the differences of the 6- and 24 h-forecast fits are not statistically significant (Fig. 15a). Degradation can be found in 6 h-forecast in the tropics, for example, around 700 hPa and below 900 hPa (Fig. 15d). The 48 h-forecast fit to the observations shows clear improvement in the lower and upper troposphere (Fig. 15a). The improvement mainly comes from the Northern Hemisphere (Fig. 15b). There is also marginal improvement around 700 hPa in the Southern

Hemisphere and near 300 hPa in the tropics. There is no significant difference between the ALLQ and the CNTL in the forecast fit to raob temperature observations (not shown) in the Northern and Southern Hemispheres. Degradation was found in the upper troposphere between 300 and 100 hPa in the tropics. Similar conclusion applies to the ALLQ_cycle_hydro experiment.

For long-term forecast, forecast scores were computed by comparing the forecast from each experiment against their own respective analyses. The upgraded all-sky framework performs better when comparing the average anomaly correlation of 500-hPa geopotential height for the period covering 26 June–31 August 2017 (Fig. 16). The improvement in the Northern Hemisphere is significant at the 95% confidence level on day 4 and day
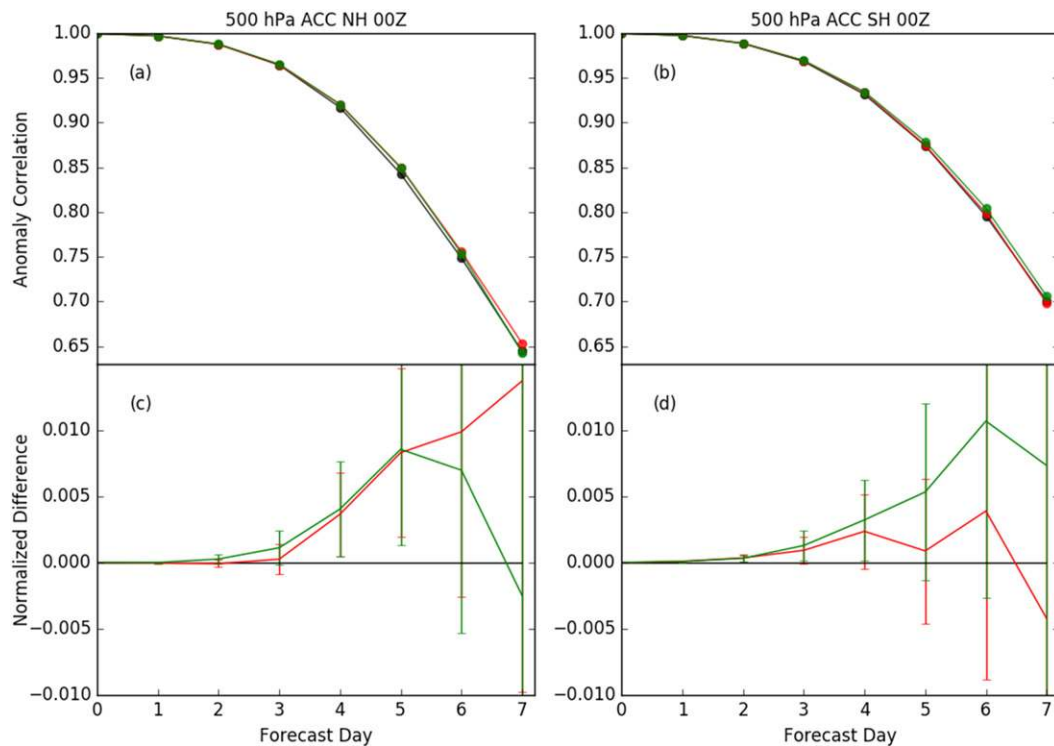
FIG. 16. (a),(b) ACC of geopotential height at 500 hPa and (c),(d) the normalized change with respect to the CNTL for ALLQ (red) and ALLQ_cycle_hydro (green) in the (left) Northern and (right) Southern Hemispheres. The forecasts were initialized at 0000 UTC and verified against their own analysis. The verification period is from 26 Jun to 31 Aug 2017. The error bars indicate the 95% confidence interval.

5 for both ALLQ and ALLQ_cycle_hydro. In the Southern Hemisphere, the improvement is significant up to day 4 when cycling the hydrometeors.

The temperature and wind vector RMS forecast errors of ALLQ and ALLQ_cycle_hydro relative to the CNTL are displayed in Figs. 17 and 18. Negative values indicate smaller RMS forecast errors relative to the CNTL, therefore, improved forecast. In terms of temperature forecast, the upgraded system shows significant improvement from day 1 to day 4 in the Southern Hemisphere and up to day 6 in the tropics in the lower troposphere at 850 hPa (Figs. 17h,i). In the Southern Hemisphere, significant improvement is also shown in short-range forecast in the middle and upper troposphere at 500 and 200 hPa (Figs. 17c,f). The results in the Northern Hemisphere is mixed. Cycling the hydrometeors is generally better or comparable to the experiment without cycling the hydrometeors in the Northern and Southern Hemispheres. The upgraded system shows some degradation in temperature forecast at 500 and 200 hPa in the tropics, while most of the differences are not statistically significant. The RMS forecast error difference of vector wind (Fig. 18) with respect to the CNTL shows similar patterns in the Northern and Southern

Hemispheres comparing to the RMS forecast error difference of temperature and the RMS error difference of the geopotential height (not shown). In the Southern Hemisphere, significant improvement can be found at 500 and 850 hPa. The impact is mixed in the Northern Hemisphere. There is no significant impact in the tropics.

The precipitation forecasts were evaluated following the fuzzy verification used in Chambon and Geer (2017) based on the method and the fractions skill score (FSS) described in Roberts and Lean (2008). The model forecast 24-h precipitation accumulations were verified against the TRMM precipitation estimates using four neighborhood sizes ranging from 25 to 200 km. Figure 19 shows the 12–36-h forecast accumulated precipitation FSSs of ALLQ and ALLQ_hydro_cycle relative to the CNTL. Some improvements can be found at 40- and 100-mm rainfall thresholds, but they are not statistically significant at the 99% confidence level. No statistically significant impact was found in longer-term precipitation forecasts (not shown).

5. Summary and future work

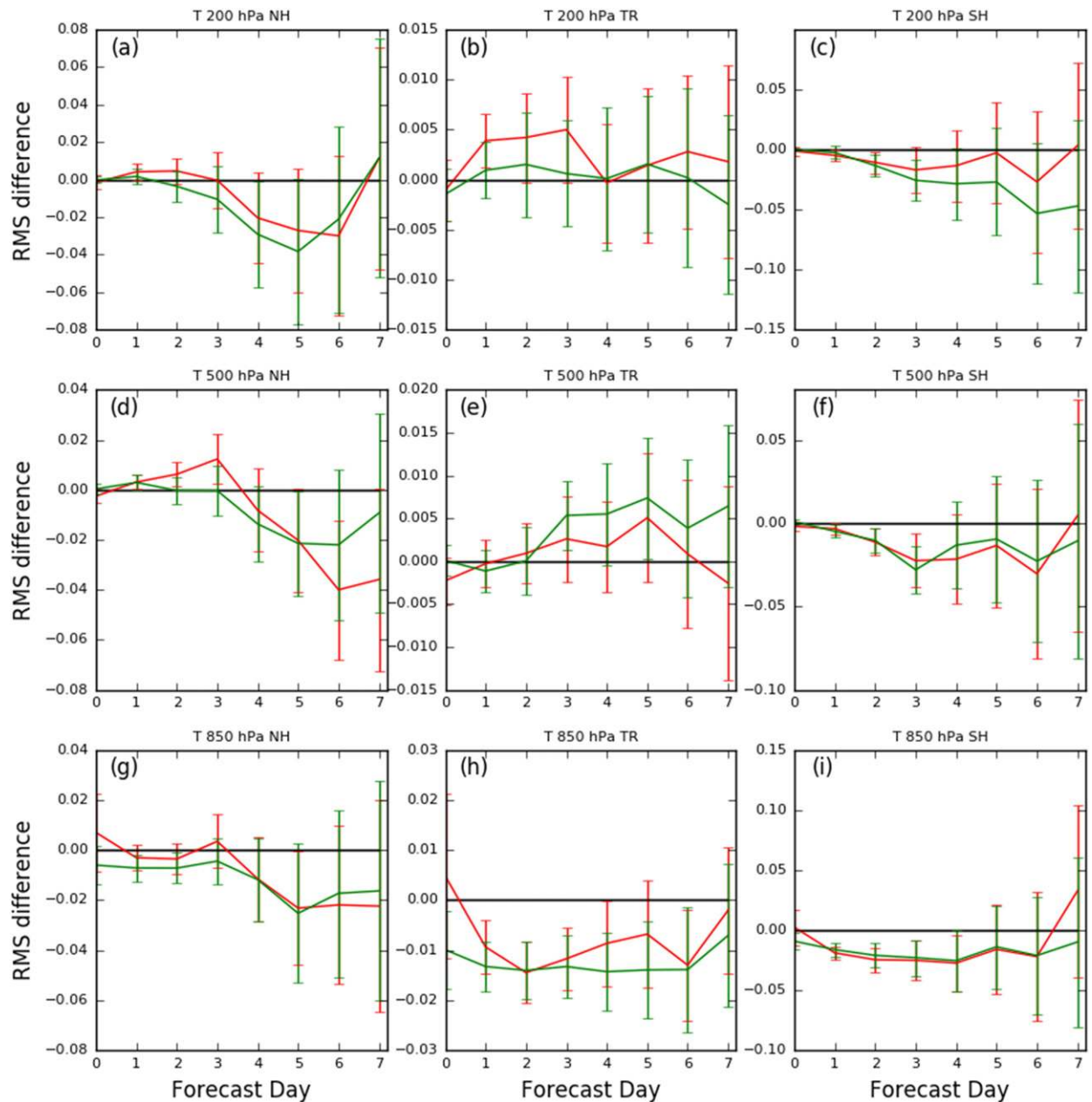The main effort of this work is to upgrade the all-sky radiance assimilation framework, in order to include the

FIG. 17. The change in temperature RMS forecast error (K) with respect to the CNTL for ALLQ (red) and ALLQ_cycle_hydro (green) in the (left) Northern Hemisphere, (center) tropics, and (right) Southern Hemisphere at (a)–(c) 200, (d)–(f) 500, and (g)–(i) 850 hPa. The verification period is from 26 Jun to 31 Aug 2017. The error bars indicate the 95% confidence interval. Reduced RMS error indicates better forecast.

full set of hydrometeors into the assimilation system for the FV3GFS. Cloud liquid water, cloud ice, rain, snow, and graupel become model prognostic variables, as the microphysics scheme has been upgraded to the more advanced GFDL microphysics scheme. The five individual hydrometeors are used as the new control variables. This upgraded all-sky assimilation framework allows the assimilation of not only cloudy, but also

precipitation-affected radiance. In this study, AMSU-A and ATMS radiances over ocean were assimilated in all-sky approach.

In the upgraded framework, precipitation screening is removed in data thinning and quality control. The latest released CRTM 2.3.0 is used to more accurately simulate microwave brightness temperature under scattering conditions. The two-column averaged cloud overlap
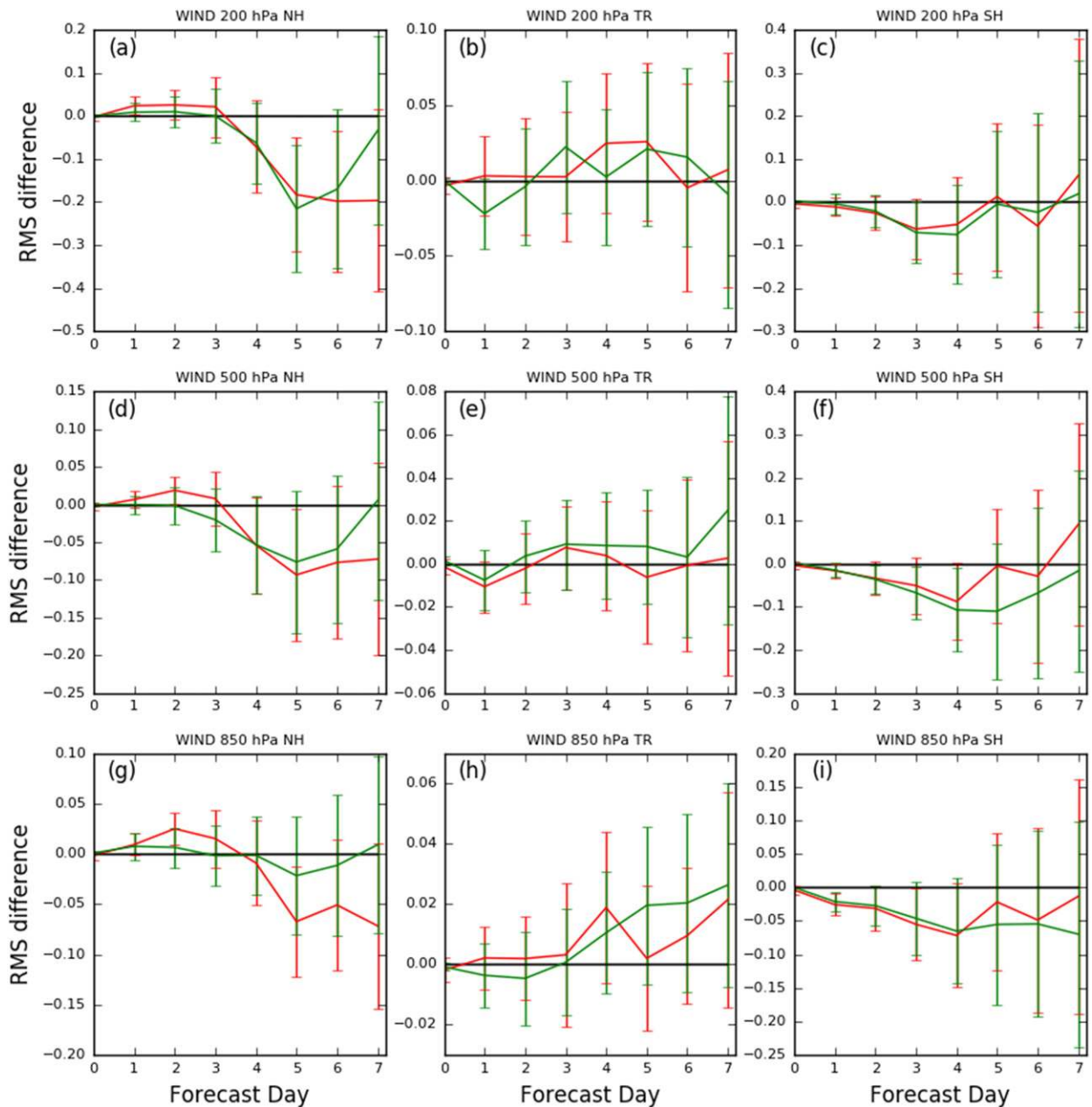
FIG. 18. As in Fig. 17, but for the wind vector RMS forecast error (m s^{-1}).

scheme is used to account for subgrid-scale cloud variability. A CRTM code error that produces negative surface emissivity Jacobian under scattering condition in surface-sensitive channels has been fixed.

An intermediate step of using individual hydrometeors as control variables is replacing the single cloud control variable CW with QL and QI directly output from the model. This change helped improve the FG fit to the observations and allowed slightly more observations to be assimilated. On the other hand, the increased

OmF bias in some areas due to this change reveals potential model bias. For example, the increased OmF positive bias near 60°S indicates that the model may have insufficient cloud liquid water and too much cloud ice in those areas. The scene is similar to what has been found in ECMWF's system years ago (Geer and Bauer 2010), which appears in cold-air outbreak region. Screening criteria (Lonitz and Geer 2015) is used to exclude observations affected by the systematic bias in ECMWF's system. Applying this screening criteria in
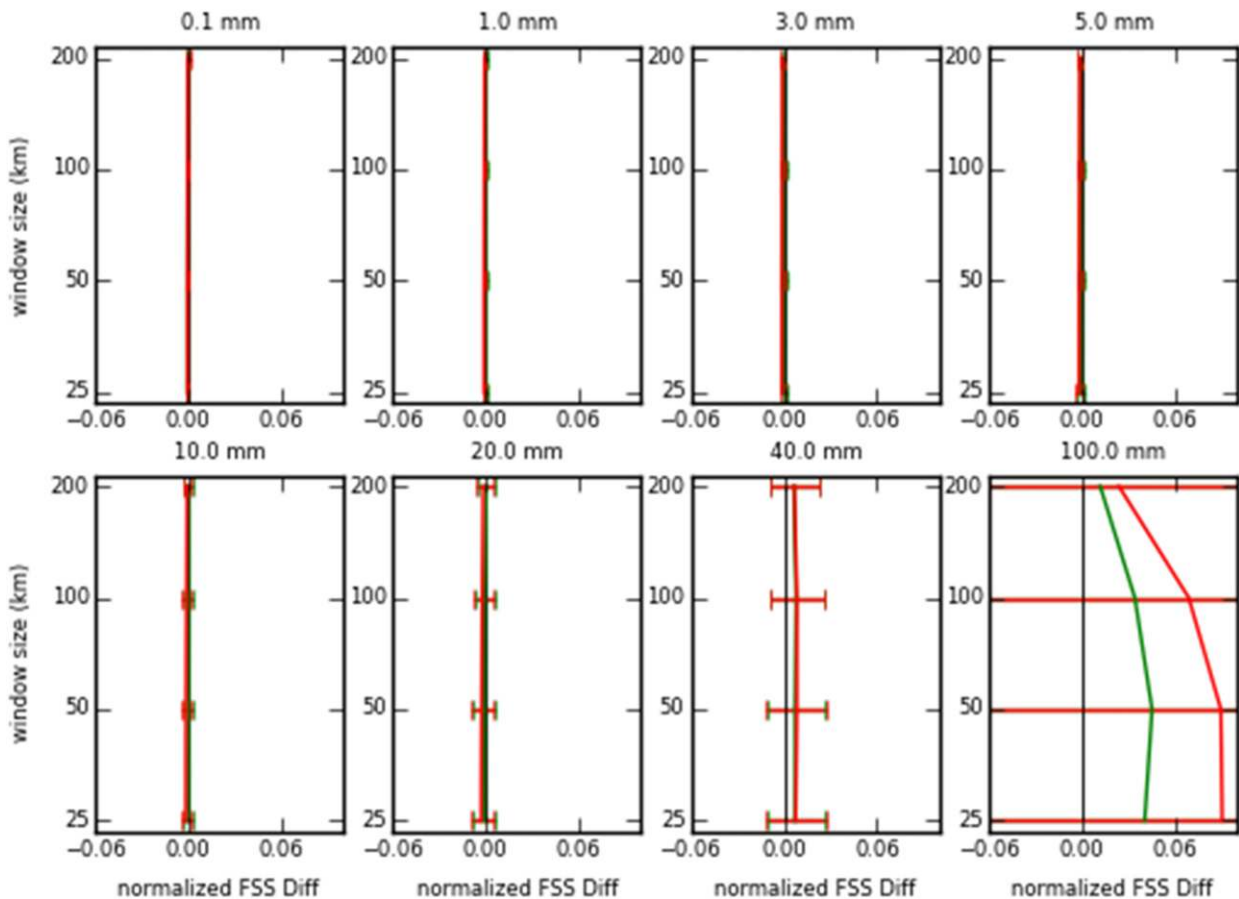
FIG. 19. Normalized differences of mean fraction skill scores of 24-h (12–36 h) accumulated precipitation forecasts verified against TRMM precipitation estimates for ALLQ (red) and ALLQ_cycle_hydro (green) with respect to the CNTL. The rainfall thresholds selected for the verification are shown at the top of the panels. The error bars indicate the 99% confidence interval.

our system will be evaluated in our future work. On the other hand, we will work with model experts to address this model bias.

Including precipitation-affected radiance in the upgraded system using all five hydrometeors as control variables generally increased the first guess departures of AMSU-A and ATMS channels sensitive to hydrometeors. In the tropical deep-convection region, including precipitating hydrometeors increased the negative OmF bias in high-frequency channels. This is likely caused by the inappropriate scattering properties of frozen hydrometeors in the CRTM LUTs. In other areas, including precipitating hydrometeors helped offset negative OmF bias in high-frequency channels. After quality control, about 1.0%–1.7% (0.7%–1.2%) more AMUS-A (ATMS) observations were assimilated. The main increase in data counts occurred in the Southern Hemisphere. The small amount of the additional observations does not reflect all the differences between the original and the new framework because a larger

amount of observations falls into the precipitation areas in the FG where multiple scattering radiative transfer is activated in the new framework.

The single cycle experiments that only assimilate AMSU-A all-sky radiances reveal that the 4DEnVar system is able to infer model dynamical fields from cloudy and precipitation-affected radiances. This is similar to the general tracing effect discussed in Geer et al. (2014). The upgraded framework provides analysis increments of precipitating hydrometeors and has impact on the magnitude of the analysis increments of other model fields, which will impact the subsequent forecast.

Overall, the upgraded all-sky assimilation system has neutral to positive impact on forecast skills. The impact on the FG fits to other observations are mostly neutral, with improvement found in the FG fit to the MHS observations. The forecast fit to radiosonde specific humidity observations is improved in the lower and upper troposphere in 48 h forecast. The 500-hPa ACC is

generally better with statistically significant improvement found in both Northern and Southern Hemispheres. Significant improvement is also seen in temperature forecast in the Southern Hemisphere and at 850 hPa in the tropics. The impact on wind forecast is generally neutral with some improvement seen in the Southern Hemisphere. The new framework has neutral impact on precipitation forecast. Cycling the hydrometeors shows comparable or sometimes better forecast skills.

This work is an initial effort on all-sky microwave radiance assimilation in the presence of precipitation in the FV3GFS. The main limitation is that precipitation-affected radiances in deep-convection regions could not be used, while those regions are often associated with high impact weather such as hurricanes. Research has been conducted to improve scattering properties of frozen hydrometers by using nonspherical particle shapes (Geer and Baordo 2014; Stegmann et al. 2018; Sieron et al. 2018). Sieron et al. (2017) constructed new CRTM LUTs based on microphysics-consistent particle size distributions. The impact of using the new CRTM LUTs based on some of these studies will be assessed. Applying the discrete dipole approximation (Draine and Flatau 1994; Liu 2008) with optimally selected particle shape for frozen hydrometeors as demonstrated in Geer and Baordo (2014) will be explored. The impact of assimilating cloudy and precipitation-affected radiance in high impact weather such as hurricanes will be investigated as the radiative transfer improves. Besides improving radiative transfer, efforts will be devoted to including convective cloud and tuning the model microphysics and/or convective schemes to improve the FG fit to the radiance observations.

REFERENCES

Bauer, P., A. J. Geer, P. Lopez, and D. Salmond, 2010: Direct 4D-var assimilation of all-sky radiances. Part I: Implementation. *Quart. J. Roy. Meteor. Soc.*, **136**, 1868–1885, https://doi.org/10.1002/qj.659.

Bormann, N., A. J. Geer, and S. J. English, 2012: Evaluation of the microwave ocean surface emissivity model FASTEM-5 in the IFS. ECMWF Tech. Memo. 667, 18 pp., https://www.ecmwf.int/en/elibrary/8303-evaluation-microwave-ocean-surface-emissivity-model-fastem-5-ifs.

Buizza, R., M. Miller, and T. N. Palmer, 1999: Stochastic representation of model uncertainties in the ECMWF ensemble prediction system. *Quart. J. Roy. Meteor. Soc.*, **125**, 2887–2908, https://doi.org/10.1002/qj.49712556006.

Chambon, P., and A. J. Geer, 2017: All-sky assimilation of Megha-Tropiques/SAPHIR radiances in the ECMWF numerical weather prediction system. ECMWF Tech. Memo. 802, 45 pp., https://doi.org/10.21957/4h085eb9.

Chen, J.-H., and Coauthors, 2019a: Advancements in hurricane prediction with NOAA's next-generation forecast system. *Geophys. Res. Lett.*, **46**, 4495–4501, https://doi.org/10.1029/2019GL082410.

——, S.-J. Lin, L. Zhou, X. Chen, S. Rees, M. Bender, and M. Morin, 2019b: Evaluation of tropical cyclone forecasts in the Next Generation Global Prediction System. *Mon. Wea. Rev.*, **147**, 3409–3428, https://doi.org/10.1175/MWR-D-18-0227.1.

Donovan, D. P., 2003: Ice-cloud effective particle size parameterization based on combined lidar, radar reflectivity, and mean Doppler velocity measurements. *J. Geophys. Res.*, **108**, 4573, https://doi.org/10.1029/2003JD003469.

Draine, B. T., and P. J. Flatau, 1994: Discrete-dipole approximation for scattering calculations. *J. Opt. Soc. Amer.*, **11**, 1491–1499, https://doi.org/10.1364/JOSAA.11.001491.

English, S. J., and T. J. Hewison, 1998: A fast generic millimeter-wave emissivity model. *Proc. SPIE*, **3503**, 288–300, https://doi.org/10.1117/12.319490.

Forbes, R., A. J. Geer, K. Lonitz, and M. Ahlgrimm, 2016: Reducing systematic errors in cold-air outbreaks. *ECMWF Newsletter*, No. 146, ECMWF, Reading, United Kingdom, 17–22, https://www.ecmwf.int/en/elibrary/17261-reducing-systematic-errors-cold-air-outbreaks.

Geer, A. J., and P. Bauer, 2010: Enhanced use of all-sky microwave observations sensitive to water vapor, cloud and precipitation. ECMWF Tech. Memo. 620, 41 pp., https://www.ecmwf.int/sites/default/files/elibrary/2010/9518-enhanced-use-all-sky-microwave-observations-sensitive-water-vapour-cloud-and-precipitation.pdf.

——, and ——, 2011: Observation errors in all-sky data assimilation. *Quart. J. Roy. Meteor. Soc.*, **137**, 2024–2037, https://doi.org/10.1002/qj.830.

——, and F. Baordo, 2014: Improved scattering radiative transfer for frozen hydrometeors at microwave frequencies. *Atmos. Meas. Tech.*, **7**, 1839–1860, https://doi.org/10.5194/amt-7-1839-2014.

——, P. Bauer, and C. W. O'Dell, 2009: A revised cloud overlap scheme for fast microwave radiative transfer. *J. Appl. Meteor. Climatol.*, **48**, 2257–2270, https://doi.org/10.1175/2009JAMC2170.1.

——, ——, and S. J. English, 2012: Assimilating AMSU-A temperature sounding channels in the presence of cloud and precipitation. ECMWF Tech. Memo. 670, 41 pp., https://www.ecmwf.int/sites/default/files/elibrary/2012/9514-assimilating-amsu-temperature-sounding-channels-presence-cloud-and-precipitation.pdf.

——, F. Baordo, N. Bormann, and S. English, 2014: All-sky assimilation of microwave humidity sounders. ECMWF Tech. Memo. 741, 57 pp., https://www.ecmwf.int/sites/default/files/elibrary/2014/9507-all-sky-assimilation-microwave-humidity-sounders.pdf.

——, and Coauthors, 2017: The growing impact of satellite observations sensitive to humidity, cloud and precipitation. *Quart. J. Roy. Meteor. Soc.*, **143**, 3189–3206, https://doi.org/10.1002/qj.3172.

——, and Coauthors, 2018: All-sky satellite data assimilation at operational weather forecasting centres. *Quart. J. Roy. Meteor. Soc.*, **144**, 1191–1217, https://doi.org/10.1002/qj.3202.

Grody, N., J. Zhao, R. Ferraro, F. Weng, and R. Boers, 2001: Determination of precipitable water and cloud liquid water

over oceans from the NOAA 15 advanced microwave sounding unit. *J. Geophys. Res.*, **106**, 2943–2953, https://doi.org/10.1029/2000JD900616.

Han, Y., P. van Delst, Q. Liu, F. Weng, B. Yan, R. Treadon, and J. Derber, 2006: JCSDA Community Radiative Transfer Model (CRTM)–Version 1. NOAA Tech. Rep. NESDIS 122, 33 pp., https://repository.library.noaa.gov/view/noaa/1157.

Hansen, J. E., and I. D. Travis, 1974: Light scattering in planetary atmospheres. *Space Sci. Rev.*, **16**, 527–610, https://doi.org/10.1007/BF00168069.

Heymsfield, A. J., and G. M. McFarquhar, 1996: High albedos of cirrus in the tropical Pacific warm pool: Microphysical interpretations from CEPEX and from Kwajalein, Marshall Islands. *J. Atmos. Sci.*, **53**, 2424–2451, https://doi.org/10.1175/1520-0469(1996)053<2424:HAOCIT>2.0.CO;2.

Ingleby, N., A. Lorenc, K. Ngan, F. Rawlins, and D. Jackson, 2013: Improved variational analyses using a nonlinear humidity control variable. *Quart. J. Roy. Meteor. Soc.*, **139**, 1875–1887, https://doi.org/10.1002/qj.2073.

Kazumori, M., and S. J. English, 2015: Use of the ocean surface wind direction signal in microwave radiance assimilation. *Quart. J. Roy. Meteor. Soc.*, **141**, 1354–1375, https://doi.org/10.1002/qj.2445.

——, and T. Kadowaki, 2017: Development of an all-sky assimilation of microwave imager and sounder radiances for the Japan Meteorological Agency global numerical weather prediction system. *21st Int. TOVS Study Conf.*, Darmstadt, Germany, International ATOVS Working Group, 1–9, https://cimss.ssec.wisc.edu/itwg/itsc/itsc21/proceedings/5.04_kazumori.pdf.

Kleist, D. T., and K. Ide, 2015: An OSSE-based evaluation of hybrid variational-ensemble data assimilation for the NCEP GFS. Part II: 4DEnVar and hybrid variants. *Mon. Wea. Rev.*, **143**, 452–470, https://doi.org/10.1175/MWR-D-13-00350.1.

——, D. F. Parrish, J. C. Derber, R. Treadon, W.-S. Wu, and S. Lord, 2009a: Introduction of the GSI into the NCEP Global Data Assimilation System. *Wea. Forecasting*, **24**, 1691–1705, https://doi.org/10.1175/2009WAF2222201.1.

——, ——, ——, ——, R. M. Errico, and R. Yang, 2009b: Improving incremental balance in the GSI 3DVar analysis system. *Mon. Wea. Rev.*, **137**, 1046–1060, https://doi.org/10.1175/2008MWR2623.1.

Lin, S.-J., 1997: A finite-volume integration method for computing pressure gradient force in general vertical coordinates. *Quart. J. Roy. Meteor. Soc.*, **123**, 1749–1762, https://doi.org/10.1002/QJ.49712354214.

——, 2004: A "vertically Lagrangian" finite-volume dynamical core for global models. *Mon. Wea. Rev.*, **132**, 2293–2307, https://doi.org/10.1175/1520-0493(2004)132<2293:AVLFDC>2.0.CO;2.

Liu, E. H., A. Collard, R. Sun, Y. Zhu, P. van Delst, D. Groff, and J. Derber, 2015: Inter comparison of CRTM and RTTOV in NCEP global model. *20th Int. TOVS Study Conf.*, Lake Geneva, WI, International ATOVS Working Group, 1–9, https://cimss.ssec.wisc.edu/itwg/itsc/itsc20/papers/8p_01_liu_paper.pdf.

——, and Coauthors, 2019: EMC contributions to CRTM development and validation. *JCSDA Quarterly*, No. 63, Joint Center for Satellite Data Assimilation, Boulder, CO, 1–9 https://doi.org/10.25923/c23x-ac34.

Liu, G., 2008: A database of microwave single-scattering properties for nonspherical ice particles. *Bull. Amer. Meteor. Soc.*, **89**, 1563–1570, https://doi.org/10.1175/2008BAMS2486.1.

Liu, Q., and F. Weng, 2006: Advanced doubling adding method for radiative transfer in planetary atmospheres. *J. Atmos. Sci.*, **63**, 3459–3465, https://doi.org/10.1175/JAS3808.1.

——, and S. Boukabara, 2014: Community Radiative Transfer Model (CRTM) applications in supporting the Suomi National Polar-Orbiting Partnership (SNPP) mission validation and verification. *Remote Sens. Environ.*, **140**, 744–754, https://doi.org/10.1016/j.rse.2013.10.011.

——, F. Weng, and S. J. English, 2011: An improved fast microwave water emissivity model. *IEEE Trans. Geosci. Remote Sens.*, **49**, 1238–1250, https://doi.org/10.1109/TGRS.2010.2064779.

Lonitz, K., and A. J. Geer, 2015: New screening of cold-air outbreak regions used in 4D-Var all-sky assimilation. EUMETSAT/ECMWF Fellowship Programme Research Rep. 35, 15 pp., https://www.ecmwf.int/en/elibrary/10777-new-screening-cold-air-outbreak-regions-used-4d-var-all-sky-assimilation.

Martin, G. M., D. W. Johnson, and A. Spice, 1994: The measurement and parameterization of effective radius of droplets in warm stratocumulus clouds. *J. Atmos. Sci.*, **51**, 1823–1842, https://doi.org/10.1175/1520-0469(1994)051<1823:TMAPOE>2.0.CO;2.

Migliorini, S., A. Lorenc, and W. Bell, 2017: A moisture-incrementing operator for the assimilation of humidity and cloud-sensitive observations: Formulation and preliminary results. *Quart. J. Roy. Meteor. Soc.*, **144**, 443–457, https://doi.org/10.1002/qj.3216.

Minamide, M., and F. Zhang, 2017: Adaptive observation error inflation for assimilating all-sky satellite radiance. *Mon. Wea. Rev.*, **145**, 1063–1081, https://doi.org/10.1175/MWR-D-16-0257.1.

Moorthi, S., H. L. Pan, and P. Caplan, 2001: Changes to the 2001 NCEP operational MRF/AVN global analysis/forecast system. NWS Tech. Procedures Bull. 484, 14 pp., http://docs.lib.noaa.gov/rescue/wb_technical_procedures_bulletin/TPB_484.pdf.

Okamoto, K., 2013: Assimilation of overcast cloudy infrared radiances of the geostationary MTSAT-1R imager. *Quart. J. Roy. Meteor. Soc.*, **139**, 715–730, https://doi.org/10.1002/qj.1994.

——, A. P. McNally, and W. Bell, 2014: Progress towards the assimilation of all-sky infrared radiances: An evaluation of cloud effects. *Quart. J. Roy. Meteor. Soc.*, **140**, 1603–1614, https://doi.org/10.1002/qj.2242.

Putman, W. M., and S.-J. Lin, 2007: Finite-volume transport on various cubed-sphere grids. *J. Comput. Phys.*, **227**, 55–78, https://doi.org/10.1016/j.jcp.2007.07.022.

Roberts, N. M., and H. W. Lean, 2008: Scale-selective verification of rainfall accumulations from high-resolution forecasts of convective events. *Mon. Wea. Rev.*, **136**, 78–97, https://doi.org/10.1175/2007MWR2123.1.

Sieron, S. B., E. E. Clothiaux, F. Zhang, Y. Lu, and J. A. Otkin, 2017: Comparison of using distribution-specific versus effective radius methods for hydrometeor single-scattering properties for all-sky microwave satellite radiance simulations with different microphysics parameterization schemes. *J. Geophys. Res. Atmos.*, **122**, 7027–7046, https://doi.org/10.1002/2017JD026494.

——, F. Zhang, E. E. Clothiaux, L. N. Zhang, and Y. Lu, 2018: Representing precipitation ice species with both spherical and nonspherical particles for radiative transfer modeling of microphysics-consistent cloud microwave scattering properties. *J. Adv. Model. Earth Syst.*, **10**, 1011–1028, https://doi.org/10.1002/2017MS001226.

Stegmann, P. G., G. Tang, P. Yang, and B. T. Johnson, 2018: A stochastic model for density-dependent microwave snow- and graupel scattering coefficients of the NOAA JCSDA Community Radiative Transfer Model. *J. Quant. Spectrosc. Radiat. Transfer.*, **211**, 9–24, https://doi.org/10.1016/j.jqsrt.2018.02.026.

Tompkins, A. M., and J. Berner, 2008: A stochastic convective approach to account for model uncertainty due to unresolved humidity variability. *J. Geophys. Res.*, **113**, D18101, https://doi.org/10.1029/2007JD009284.

van Delst, P., E. H. Liu, and L. Bi, 2016: Cloud fraction in the CRTM. JCSDA Office Note CRTM-4, Rrev. 71147, 36 pp.

Wang, X., and T. Lei, 2014: GSI-based four-dimensional ensemble–variational (4DEnsVar) data assimilation: Formulation and single-resolution experiments with real data for the NCEP Global Forecast System. *Mon. Wea. Rev.*, **142**, 3303–3325, https://doi.org/10.1175/MWR-D-13-00303.1.

Weng, F., L. Zhao, R. R. Ferraro, G. Poe, X. Li, and N. C. Grody, 2003: Advanced Microwave Sounding Unit cloud and precipitation algorithms. *Radio Sci.*, **38**, 8086, https://doi.org/10.1029/2002RS002679.

Whitaker, J. S., and T. M. Hamill, 2002: Ensemble data assimilation without perturbed observations. *Mon. Wea. Rev.*, **130**, 1913–1924, https://doi.org/10.1175/1520-0493(2002)130<1913:EDAWPO>2.0.CO;2.

——, and ——, 2012: Evaluating methods to account for system errors in ensemble data assimilation. *Mon. Wea. Rev.*, **140**, 3078–3089, https://doi.org/10.1175/MWR-D-11-00276.1.

——, ——, X. Wei, Y. Song, and Z. Toth, 2008: Ensemble data assimilation with the NCEP Global Forecast System. *Mon. Wea. Rev.*, **136**, 463–482, https://doi.org/10.1175/2007MWR2018.1.

Zhao, Q., and F. H. Carr, 1997: A prognostic cloud scheme for operational NWP models. *Mon. Wea. Rev.*, **125**, 1931–1953, https://doi.org/10.1175/1520-0493(1997)125<1931:APCSFO>2.0.CO;2.

Zhou, L., S. Lin, J. Chen, L. Harris, X. Chen, and S. Rees, 2019: Toward convective-scale prediction within the Next Generation Global Prediction System. *Bull. Amer. Meteor. Soc.*, **100**, 1225–1243, https://doi.org/10.1175/BAMS-D-17-0246.1.

Zhu, Y., J. Derber, A. Collard, D. Dee, R. Treadon, G. Gayno, and J. A. Jung, 2014a: Enhanced radiance bias correction in the National Centers for Environmental Prediction's Gridpoint Statistical Interpolation data assimilation system. *Quart. J. Roy. Meteor. Soc.*, **140**, 1479–1492, https://doi.org/10.1002/qj.2233.

——, and Coauthors, 2014b: Variational bias correction in the NCEP's data assimilation system. Preprints, *19th Int. TOVS Study Conf.*, Jeju Island, South Korea, International ATOVS Working Group, 10.02, http://cimss.ssec.wisc.edu/itwg/itsc/itsc19/program/papers/10_02_zhu.pdf.

——, and Coauthors, 2016: All-sky microwave radiance assimilation in NCEP's GSI analysis system. *Mon. Wea. Rev.*, **144**, 4709–4735, https://doi.org/10.1175/MWR-D-15-0445.1.

——, G. Gayno, R. J. Purser, X. Su, and R. Yang, 2019: Expansion of the all-sky radiance assimilation to ATMS at NCEP. *Mon. Wea. Rev.*, **147**, 2603–2620, https://doi.org/10.1175/MWR-D-18-0228.1.